The Astrophysical Journal, 962:97 (18pp), 2024 February 10 https://doi.org/10.3847/1538-4357/ad0bed

Quantifying the Transit Light Source Effect: Measurements of Spot Temperature and Coverage on the Photosphere of AU Microscopii with High-resolution Spectroscopy and Multicolor Photometry

William C. Waalkes[1,2,7], Zachory K. Berta-Thompson[1], Elisabeth R. Newton[2], Andrew W. Mann[3], Peter Gao[4], Hannah R. Wakeford[5], Lili Alderson[5], and Peter Plavchan[6]
[1] Department of Astrophysical & Planetary Sciences, University of Colorado Boulder, 2000 Colorado Ave., Boulder, CO 80309, USA
[2] Department of Physics and Astronomy, Dartmouth College, Hanover, NH 03755, USA
[3] Department of Physics and Astronomy, The University of North Carolina at Chapel Hill, Chapel Hill, NC 27599-3255, USA
[4] Earth and Planets Laboratory, Carnegie Institute of Washington, Washington, DC, USA
[5] School of Physics, University of Bristol, Bristol, UK
[6] Department of Physics and Astronomy, George Mason University, Fairfax, VA 22030, USA
Received 2023 August 9; revised 2023 October 20; accepted 2023 October 23; published 2024 February 9

Abstract

AU Microscopii (AU Mic) is an active 24 ± 3 Myr pre-main-sequence M dwarf in the stellar neighborhood ($d = 9.7$ pc) with a rotation period of 4.86 days. The two transiting planets orbiting AU Mic, AU Mic b and c, are warm sub-Neptunes on 8.5 and 18.9 day periods and are targets of interest for atmospheric observations of young planets. Here we study AU Mic's unocculted starspots using ground-based photometry and spectra in order to complement current and future transmission spectroscopy of its planets. We gathered multicolor Las Cumbres Observatory (LCO) 0.4 m SBIG photometry to study the star's rotational modulations and LCO Network of Robotic Echelle Spectrographs high-resolution spectra to measure the different spectral components within the integrated spectrum of the star, parameterized by three spectral components and their coverage fractions. We find AU Mic's surface has at least two spectral components: a $T_{\rm amb} = 4003^{+15}_{-14}$ K ambient photosphere and cool spots that have a temperature of $T_{\rm spot} = 3003^{+63}_{-71}$ K, covering a globally averaged area of $39\% \pm 4\%$ which increases and decreases by $5.1\% \pm 0.3\%$ from the average throughout a rotation. We also detect a third flux component with a filling factor less than 0.5% and a largely uncertain temperature between 8500 and 10,000 K that we attribute to flare flux not entirely omitted when time averaging the spectra. We include measurements of spot characteristics using a two-temperature model, which we find agree strongly with the three-temperature results. Our expanded use of various techniques to study starspots will help us better understand this system and may have applications for interpreting the transmission spectra for exoplanets transiting stars of a wide range of activity levels.

Unified Astronomy Thesaurus concepts: Starspots (1572); M dwarf stars (982); Pre-main sequence stars (1290); Stellar rotation (1629); Exoplanet atmospheres (487); Transits (1711); Multicolor photometry (1077); High resolution spectroscopy (2096)

Supporting material: figure sets

1. Introduction

Observations from JWST are now revealing exoplanet atmospheres in more detail than ever before (Fu et al. 2022; Ahrer et al. 2023; Alderson et al. 2023; Feinstein et al. 2023; Rustamkulov et al. 2023) using an observational technique called transmission spectroscopy (Seager & Sasselov 2000; Brown et al. 2001; Pont et al. 2007; Sing et al. 2011; Berta et al. 2012). Transmission spectroscopy is done by measuring the transit depth (which is a proxy for the planet's radius) of an exoplanet as a function of wavelength and inferring atmospheric absorption (e.g., Seager & Sasselov 2000) and/or scattering (e.g., Robinson et al. 2014; Sing et al. 2016) at wavelengths where the planet's transit is deeper. The stellar photons that are absorbed by the planet and its atmosphere originate specifically from the transit chord, the swathe of stellar surface occulted by the planet which in general is indistinguishable from the surrounding photosphere except in compact systems which exhibit transits at multiple latitudes. Stellar surfaces can be homogeneous (i.e., spatially "smooth" aside from granulation and limb-darkening effects), in which case the chord spectrum is the same as the disk-integrated spectrum, or they can be heterogeneous (containing active regions), in which case the transit chord is not necessarily representative of the disk-integrated stellar spectrum.

A homogeneous stellar background surface has typically been adopted in transmission studies. While this assumption holds true in some cases, most stars do not have smooth, single-temperature surfaces but are instead spotted with activity-induced heterogeneities. Spots are created where magnetic field lines pass through the photosphere and the magnetic pressure overwhelms the local gas pressure, suspending convection and causing the region within the intersecting field to cool. Faculae arise from weaker concentrations of field lines where this pressure is not enough to suspend convection but is enough to reduce the local opacity and increase the flux emanating from deeper in the photosphere, creating a brightening effect (Basri 2021).

[7] NSF Graduate Research Fellow.

A nonaxisymmetric distribution of spots and faculae creates time- and wavelength-dependent changes in the stellar surface flux, which has been observed in high-resolution stellar spectra (Wing et al. 1967; Afram & Berdyugina 2015), color–magnitude relations (Vogt 1979; Olah et al. 1997), stellar rotational modulation (Vogt 1979; Pass et al. 2023), and more recently in exoplanet transits (Brown et al. 2001; Pont et al. 2008; Sanchis-Ojeda & Winn 2011; Sing et al. 2011). When spots or faculae lie on the transit chord and are occulted by transiting planets, they create bumps or dips in the transit light curve that can bias the exoplanet radius measurement. Occulted active regions, provided they occupy discrete regions of the transit chord and their flux contrast appears above the noise, show up directly in transit light curves and can be identified and removed from the measured transmission spectrum. Unocculted active regions, however, alter the disk-averaged spectrum such that it is no longer representative of the true source spectrum of photons entering the planetary atmosphere. This in turn creates spurious wavelength-dependent changes to the exoplanet transit depth in what is now known as the transit light source effect (TLSE; Rackham et al. 2018, 2019).

On cool stellar surfaces (below about 4000 K), molecular absorption lines (like H_2O, VO, and TiO; Jones et al. 1995; Allard et al. 2012) begin to appear in the stellar spectrum and become entangled with molecular absorption signals in planetary atmospheres. Cool unocculted spots with different or deeper molecular absorption lines than the surrounding photosphere will appear to add molecular absorption at those wavelengths in planetary transmission spectra and lead to mischaracterization of exoplanets and their atmospheres. Additionally, unocculted spots give rise to an increasing transit depth toward bluer wavelengths as their contrast against the surrounding photosphere increases, which can be mistakenly identified as Rayleigh scattering in a transiting exoplanet's atmosphere (e.g., Robinson et al. 2014). Until we can precisely and reliably determine spot characteristics on our host stars, the signature of exoplanet atmospheres will be very challenging or impossible to disentangle from spot contamination for nearly all transmission observations of exoplanets around M and K dwarfs. This degeneracy, exemplified in recent transmission observations of sub-Neptune exoplanets TOI 270d (Mikal-Evans et al. 2023), Gl 486b (Moran et al. 2023), K2-33b (Thao et al. 2023), L 98-59c (Barclay et al. 2023), and the temperate terrestrial exoplanet TRAPPIST-1b (Lim et al. 2023) is what we aim to mitigate for transmission observations of AU Microscopii (AU Mic) b by precisely measuring spot characteristics for its host star in this work.

1.1. AU Microscopii

AU Mic (Torres & Ferraz Mello 1973) is a nearby (9.7 pc; Gaia Collaboration et al. 2023), young (24 ± 3 Myr; Mamajek & Bell 2014), rapidly rotating ($P_{\rm rot} = 4.86$ days; Plavchan et al. 2020; Donati et al. 2023) pre-main-sequence M dwarf with a debris disk (Kalas et al. 2004; Chen et al. 2005; MacGregor et al. 2013). This star has an inflated radius as it settles onto the main sequence, with $M = 0.60\ M_\odot$ and $R = 0.82\ R_\odot$ (Donati et al. 2023) and an effective temperature of 3600–3700 K (e.g., Afram & Berdyugina 2019; Plavchan et al. 2020; Cristofari et al. 2023) There are two transiting warm Neptunes on 8.46 and 18.86 day periods (Hirano et al. 2020; Plavchan et al. 2020; Martioli et al. 2021; Gilbert et al. 2022; Zicher et al. 2022) and two unconfirmed candidate nontransiting planets on 12.74 and 33.39 day periods recently discovered through transit timing variations and radial velocity analysis (Wittrock et al. 2022; Donati et al. 2023; Wittrock et al. 2023). The existence of an observable debris disk with interior transiting planets is a rare and exciting architecture that holds vast scientific potential.

Table 1
System Parameters Relevant to This Study

Quantity	Value
AU Mic	
D [pc]	9.714 ± 0.002 (a)
$T_{\rm eff}$ [K]	3665 ± 31 (b)
M_* [$M_\odot$]	0.60 ± 0.03 (c)
R_* [$R_\odot$]	0.82 ± 0.05 (c)
$P_{\rm rot}$ [days]	4.86 ± 0.005 (c), (d)
Metallicity [dex]	0.12 ± 0.10 (c)
log g [$\log_{10}$(cm s^{-2})]	4.52 ± 0.05 (c)
AU Mic b	
P [days]	8.4631427 (e)
R_p/R_*	0.0433 ± 0.0017 (e)

References. (a) Gaia Collaboration et al. (2023), (b) Cristofari et al. (2023), (c) Donati et al. (2023), (d) Martioli et al. (2021), and (e) Szabó et al. (2022).

Furthermore, this system is one of the best cases we have for studying star–planet interactions and the effects of young M dwarf activity on planetary atmospheres, an issue of great interest and concern in the search for terrestrial atmospheres and potentially habitable planets orbiting M dwarf stars (e.g., Shields et al. 2016; Louca et al. 2023). This star's frequent high-energy flaring that may eventually lead to photoevaporation of the atmospheres of AU Mic b and c (Feinstein et al. 2022) and even in the case where the atmospheres are preserved, the long-term implications of young M dwarf activity on planetary habitability are ominous. By continuing to study AU Mic and its planets, we can build an internally consistent understanding of a nearby multiplanet system in the early stages of formation with a stellar surface evolving on months-long timescales (e.g., Donati et al. 2023). System parameters are summarized in Table 1 and a thorough review of AU Mic's stellar and planetary characteristics can be found in Donati et al. (2023).

1.2. Transmission Observations of AU Mic b

The observations we present in this work are part of a companion study alongside Hubble Space Telescope (HST)/WFC3 transmission spectra of AU Mic b; the first on 2021 August 30 (BJD 2459455.98) and the second on 2022 April 14 (BJD 2459684.40). Because AU Mic's spots evolve over time (e.g., Szabó et al. 2021, 2022; Gilbert et al. 2022), we have collected photometric and spectroscopic observations contemporaneous with the WFC3 observations to provide constraints on spot contamination at the time of both transmission visits. These transmission spectra will be analyzed in the context of our results and presented in a subsequent paper.

1.3. Objectives and Layout

In order to characterize AU Mic's spots and forward model the spot contamination level in AU Mic b's transmission spectrum, we assembled a self-consistent statistical framework that combines multicolor time-series photometry with contemporaneous high-resolution spectroscopy. This method

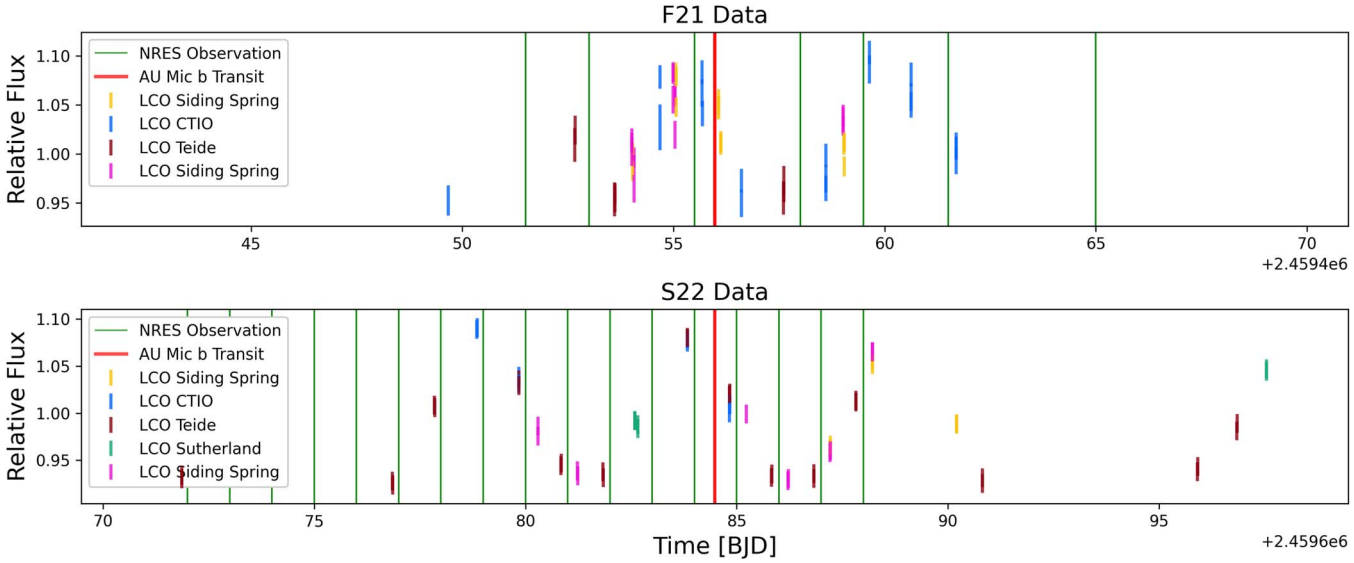

Figure 1. Processed and baseline-corrected photometry data for all filters in visits F21 (top) and S22 (bottom) with vertical markers showing the temporal distribution of WFC3 (red) and NRES (green) observations. The color of each photometric data point is based on the LCO site where those data were observed. The time between transit observations is 229 days.

allows us to break observational degeneracies between spot coverage and spot contrast and better understand the *bulk* characteristics of AU Mic's spots. We use *bulk* to mean the spatially unresolved flux-weighted characteristics based on the treatment of spots as discrete regions without complex temperature profiles, ignoring for example the distinction between umbra and penumbra. These are heavy assumptions, but we argue that our models are appropriate for the quality of our data and the information we hope to obtain.

This paper is laid out as follows: in Section 2 we describe the types of observations used in the spot analysis and the specific observations we acquired, along with the data reduction and processing. In Section 3 we describe our methods of analyzing AU Mic's rotational modulations (Section 3.1), assembling the self-consistent statistical framework for modeling spot filling factor and temperature (Section 3.2), and forward modeling the spot contamination in AU Mic b's transmission spectrum (Section 3.3). In Section 4 we report the results of our spot model and in Section 5 we discuss the physical implications of our results, how they compare to previous studies, and the limitations of our approach.

2. Observations and Data Reduction

2.1. Observing Spots

Starspot characteristics are difficult to disentangle in practice as there is a degeneracy between spot coverage and temperature contrast that creates similar observational effects within a single wave band. In addition, the physics and structure of stellar surfaces is poorly understood for all but the most heavily studied stars. Stars of different type, rotation rate, and magnetic field strength exhibit differing forms of surface phenomena which are or will eventually be relevant to understand for the future of exoplanet discovery and characterization.

Breaking spot degeneracies can be done by combining observations across optical and infrared wavelengths. Short-wavelength broadband photometry allows us to probe starspots where they stand out the most against the stellar background (higher flux contrast toward the Wien limit), while long-wavelength observations are useful for identifying the molecular characteristics of starspots where they overlap with planetary atmospheric absorption. Broadband photometric variability measurements help us probe different temperature components on rotating stars, but generally only provides a lower limit on the total spot coverage due to unknown axisymmetries in spot distribution (Apai et al. 2018). Photometric variability amplitudes decrease with wavelength as the two flux components approach the Rayleigh–Jeans limit, so measuring rotational variability across the optical to the infrared provides strong constraints on the spot-to-photosphere temperature contrast (e.g., Strassmeier & Olah 1992).

High-resolution, time-series spectra have been used to study the relationships between stellar activity tracers and spot coverage (e.g., Schöfer et al. 2019; Medina et al. 2022). For spectroscopic studies, stellar spectra are modeled as a combination of two or more temperature components (often referred to as spectral decomposition; e.g., Gully-Santiago et al. 2017; Zhang et al. 2018; Wakeford et al. 2019). Specific molecular lines are often used as spot tracers including TiO (Wing et al. 1967; Vogt 1979), CaH, MgH, FeH, and CrH (e.g., Neff et al. 1995; Afram & Berdyugina 2019). We recommend Berdyugina (2005), Apai et al. (2018), and Rackham et al. (2018) for more thorough reviews of starspots and the techniques used to study them.

2.2. Data

We acquired Las Cumbres Observatory (LCO) 0.4 m g'-, r'-, and i'-band[8] SBIG photometry and Network of Robotic Echelle Spectrographs (NRES) high-resolution echelle spectra on two separate visits spanning 2–3 weeks around their respective transmission observations (occurring in fall of 2021 and spring of 2022, hereafter F21 and S22, respectively). These data were acquired contemporaneously with observations of AU Mic b's HST/WFC3 transmission spectrum (see Figure 1) with the hope of precisely constraining the magnitude of spot contamination at the appropriate stellar epoch and phase.

[8] https://lco.global/observatory/instruments/filters/

2.2.1. SBIG Imaging

Photometry was acquired between 2021 August 12 and 2021 September 3 (F21) and 2022 April 1 and 2022 April 27 (S22) using five separate telescopes automatically scheduled depending on weather, telescope availability, and target observability. Typical exposure times were 20 s in g', 10 s in r', and 6 s in i'. The photometric data were automatically reduced into calibrated images by the BANZAI pipeline (McCully et al. 2022) and downloaded from the LCO Science Archive.[9] We performed aperture photometry with AstroImageJ's multiaperture photometry tool (Collins et al. 2017). For each filter, the same three comparison stars are used to account for local atmospheric effects throughout the night and measure the target star's relative flux. The fact that AU Mic is far brighter than its nearby comparison stars (g', r', and i' magnitudes of 9.579 ± 0.05, 8.636 ± 0.09, and 7.355 ± 0.14, respectively; Zacharias et al. 2012) means that the photon noise in the photometry is set by the comparison star brightness, rather than by AU Mic itself. Scintillation also contributes significantly to the photometric noise budget, particularly in the i' photometry where exposure times are very short to avoid AU Mic saturating. After performing aperture photometry, the signal-to-noise ratio (S/N) per exposure was 300–600 in F21 g' and r', 200–300 in F21 i', and 500–1000 in S22 g' and r'. For the first visit (F21), we have 450 exposures in Sloan Digital Sky Survey (SDSS) g', 1036 exposures in r', and 1175 in i'. For the second visit (S22) we have 328 in g' and 330 in r'.

For each night of observations, we stitch together all data in a single filter and take the median in order to minimize the effect of flares. We use `scipy.optimize` to fit an initial sinusoid model for sigma clipping. We clip 10σ outliers from the initial model to account for flux variations outside of the rotational modulation (i.e., flares), generate an optimized fit with `scipy.optimize.minimize`, clip 5σ outliers from that model, reoptimize a final time, and normalize the uncertainties based on the reduced χ^2 statistic from this final optimized fit. The first cutoff is set at 10σ because after median binning, the uncertainties were underestimated and a slightly wrong initial model could easily exclude otherwise useful data. The second cutoff is set at 5σ to account for any extreme outliers still remaining without being too restrictive, accounting for known uncertainties in the chosen model. After processing, the typical per-night S/N was 70–100 for g' and r' and 30–50 in i', with a total of 19 data points for F21 g', 18 for r', 17 for F21 i', 28 data points for S22 g', and 30 for S22 r'. The per-night S/N only reaches to 100 because we set a minimum uncertainty of 1% on the postprocessing photometry based on the per-night spread in flux.

2.2.2. NRES Spectra

AU Mic's spectrum was observed in the 0.39–0.91 μm NRES bandpass with 600 s exposure times resulting in a total of 38 observations from 2021 August 24 to 2021 September 09 (F21) and 48 observations from 2022 April 2 to 2022 April 18 (S22). The $R = 53{,}000$ NRES spectra were reduced by the BANZAI-NRES pipeline (McCully et al. 2022) and downloaded from the LCO Science Archive. Spectra from individual observations show typical peak S/Ns of 35 where the star is brightest (around order 60) and drops off to below 10 in order 52 and beyond order 83, so we omit orders outside of this range from our analysis. We processed the spectra with the `chromatic`[10] tool, first correcting for the velocity shift in each order's spectra from the movement of the Earth in different positions of its orbit. This was -9.5 km s^{-1} in F21 and 33.0 km s^{-1} in S22, derived from a χ^2 grid search using a single-temperature optimized model spectrum and `scipy.optimize.minimize`. We median-combine spectra in time to one averaged spectrum per night resulting in seven spectra in F21 and 17 spectra in S22. We also bin each spectrum to 0.05 nm (roughly $R = 11{,}000$–$18{,}000$); this is greater than the Doppler broadening width of 0.015–0.024 nm that we estimate for the NRES bandpass based on AU Mic's $v\sin i$ of 8–9 km s^{-1} (e.g., Donati et al. 2023). Zeeman broadening is an additional effect which alters line profiles in magnetically active stars (e.g., Gray 1984), but we calculate the Zeeman broadening (Reiners et al. 2013) to be less than rotational broadening at these wavelengths and accounted for within our chosen bin size. Many of our spectral orders overlap with absorption bands in Earth's atmosphere so we trim out any wavelengths where the molecular line transmission fraction of the atmosphere is <0.995 (i.e., any wavelength at which $\geqslant 0.5\%$ of the photons are absorbed) based on time-averaged telluric data from Skycalc (Noll et al. 2012; Jones et al. 2013). We run a sigma-clipping routine that first calculates an optimized single-temperature PHOENIX model (Husser et al. 2013) for each spectrum, and second clips emission lines, defined as points $>3\sigma$ above the optimized model. Uncertainties on the time-averaged spectra are inflated to give a reduced χ^2 of 1 when fit against a 3650 K template. This is an increase in uncertainty of 7–55x depending on the order, resulting in typical per-order S/N of 10–40.

After processing, we omitted two-thirds of the spectral orders from the final analysis based on their level of telluric overlap or in some cases because the ambient or spotted component was very poorly constrained, possibly due to the spectral model fidelity problem (Iyer & Line 2020; Rackham & de Wit 2023). The orders we include in the final analysis are 53, 54, 59, 61, 69, 71, 72, 75, 76, 81, 82, and 83, with details given in Table 2. In F21, there are total of 1831 spectral data points, with 1828 in S22, for a total of 3659 spectral data points. Discussion on the choice of orders to include and spectral model results for each individual order is given in the Appendix.

3. Methods

Our analysis is ordered in three steps:

1. Measuring the stellar rotation signal, where photometric data are modeled as a sine wave to infer the semiamplitude of stellar variability.
2. Modeling spot characteristics, where we infer spot characteristics based on AU Mic's $T_{\rm eff}$, measured photometric variabilities, and the time-averaged spectra. This is the primary focus of our analysis.
3. Forward modeling the TLSE, where we take the posterior samples from our modeling to calculate the range of spectral contamination we can expect in the HST/WFC3 transmission data for AU Mic b.

Figure 2 shows a cartoon of the stellar surface we model as a combination of ambient photosphere with a characteristic spectrum $S(\lambda, T_{\rm amb})$ and spots with characteristic spectra $S(\lambda, T_{\rm spot})$ covering a globe-averaged $f_{\rm spot}$ which deviates from the average coverage by

[9] https://archive.lco.global/

[10] https://github.com/zkbt/chromatic

$\pm\Delta f_{\rm spot}$ throughout the stellar rotation. We include a third flux component (not shown on the figure) and label this component "hot" (with attributes $f_{\rm hot}$ and $T_{\rm hot}$) as we are uncertain about the physical source of the measured hot component, if it exists. The primary results we report in Section 4 come from this three-temperature modeling, but we also test a two-temperature model and discuss its results and implications in Section 5. The two visits are modeled with the same set of parameters (implying no change to the surface components between visits), an assumption we test and discuss later in the paper.

3.1. Measuring Photometric Variability

Once the photometry data were processed as described in Section 2, we measure the rotational variability with a sinusoidal model with the following form:

$$F(t) = A\sin(2\pi t/P) + B\cos(2\pi t/P) + C_k, \quad (1)$$

where t is the time of an individual data point, P is the stellar rotation period which we keep fixed at 4.86 days, A and B are amplitude parameters, and $C_{\rm k}$ is the offset parameter unique to each camera in each visit. We fit each camera's data separately as we expect different cameras to have slightly different responses and should be normalized to their separate average fluxes. While AU Mic has a notably asymmetric light curve (e.g., the TESS light curves shown in Martioli et al. 2021) and Angus et al. (2018) caution against using simple sinusoidal models to fit stellar rotation curves, our goal here is not to infer a precise rotation curve morphology and spot distribution but to measure the relative amplitude of flux variability between separate bandpasses.

Using `emcee` (Foreman-Mackey et al. 2013), we ran Markov Chain Monte Carlo (MCMC) sampling with 100 walkers, 1000 steps, and 25% burn-in. We used the autocorrelation time to judge when the sampler had converged for each parameter (e.g., Goodman & Weare 2010). Median-value parameters and their 1σ uncertainties calculated from the sample distributions are propagated through to the following reformulation of Equation (1):

$$F(t) = X\sin(2\pi t/P + \theta) + C_k, \quad (2)$$

where $X = \sqrt{A^2 + B^2}$ and $\theta = \arccos(A/X)$. X is the photometric semiamplitude of variability (or $\frac{\Delta S}{S_{avg}}$) for a given photometric bandpass, which we use as input for the spot characteristics model described below. We inflate the uncertainty on each variability measurement by 25% to account for the assumptions of a simple rotation curve and negligible facular contribution.

3.2. Spot Characteristics Model

To draw inferences about AU Mic's spot and facula characteristics, we assembled a model for three data components: the effective temperature, $T_{\rm eff}$, the photometric semiamplitude of variability, $\frac{\Delta S}{S_{\rm avg}}$, and the time-averaged stellar spectrum, $S_{\rm avg}$. Each of these components is modeled as a function of some combination of $f_{\rm hot}$, $f_{\rm spot}$, $T_{\rm hot}$, $T_{\rm spot}$, and $T_{\rm amb}$, with the model priors described in Table 3.

Modeling photometric variability requires one additional parameter, the |peak – average| amplitude of the change in spot coverage throughout a rotation, $\Delta f_{\rm spot}$. This parameter represents a change in spot coverage relative to the average coverage in a way that is not relevant to our models of the time-averaged spectral data or $T_{\rm eff}$. It can range from 0, where the surface is homogeneous or the surface features are distributed symmetrically around the rotation axis, to $\Delta f_{\rm spot} = f_{\rm spot}$, where the total spot coverage is clustered on the surface such that it rotates entirely in and out of view. While photometric variabilities only provide a lower limit on the *average* spot coverage fraction, the magnitude of variability depends strongly on this change in spot coverage throughout a rotation and can be precisely constrained with sufficient evidence of the spectral contrast between the ambient and spotted photosphere.

Table 2
Details of the NRES Echelle Spectra Acquired for This Study

Order	λ (μm)	Note
53*	0.873–0.888	TiO line [8860 Å]
54	0.858–0.872	⋯
55	0.842–0.857	Excluded—telluric contamination
56	0.826–0.841	Excluded—telluric contamination
57	0.810–0.826	Excluded—telluric contamination
58	0.798–0.812	Excluded—telluric contamination
59*	0.784–0.798	⋯
60	0.771–0.784	Excluded—poor fit
61*	0.759–0.772	TiO line [7600 Å]
62	0.746–0.760	Excluded—poor fit
63	0.734–0.748	Excluded—telluric contamination
64	0.723–0.736	Excluded—telluric contamination
65	0.712–0.724	Excluded—telluric contamination | TiO line [7150 Å]
66	0.701–0.713	Excluded—telluric contamination | TiO line [7050 Å]
67	0.690–0.702	Excluded—telluric contamination
68	0.680–0.692	Excluded—telluric contamination
69*	0.671-0.682	⋯
70	0.661–0.672	Excluded—poor fit
71*	0.652–0.663	Hα band
72*	0.642–0.653	⋯
73*	0.634–0.645	Excluded—poor fit
74	0.625–0.636	Excluded—telluric contamination
75*	0.617–0.627	⋯
76*	0.609–0.619	⋯
77	0.601–0.611	Excluded—poor fit
78	0.593–0.603	Excluded—telluric contamination
79	0.586–0.596	Excluded—telluric contamination
80	0.578–0.588	Excluded—poor fit
81*	0.571–0.581	⋯
82*	0.564–0.574	⋯
83*	0.558–0.567	⋯

Note. The full spectrum spans 0.39–0.91 μm (orders 119–52) but we truncate the table and the analysis at orders 53 and 83 to focus on orders which are not dominated by noise. Orders that we omit from the final analysis are noted with a brief explanation, and further discussion of modeling specific orders is provided in the Appendix. Most omitted orders were heavily contaminated by telluric absorption, whereas the orders labeled "poor fit" typically exhibit extremely cold spots, at the limit of the spectral library. Note that wavelength decreases with order.

3.2.1. Effective Temperature

Similar to Libby-Roberts et al. (2022), we treat $T_{\rm eff}$ in the following form:

$$T_{\rm eff}^4 = f_{\rm spot}\,T_{\rm spot}^4 + f_{\rm hot}\,T_{\rm hot}^4 + f_{\rm amb}\,T_{\rm amb}^4, \quad (3)$$

where $f_{\rm spot}$ is the globally averaged spot coverage fraction with temperature $T_{\rm spot}$, $f_{\rm hot}$ is the average coverage of any potential third

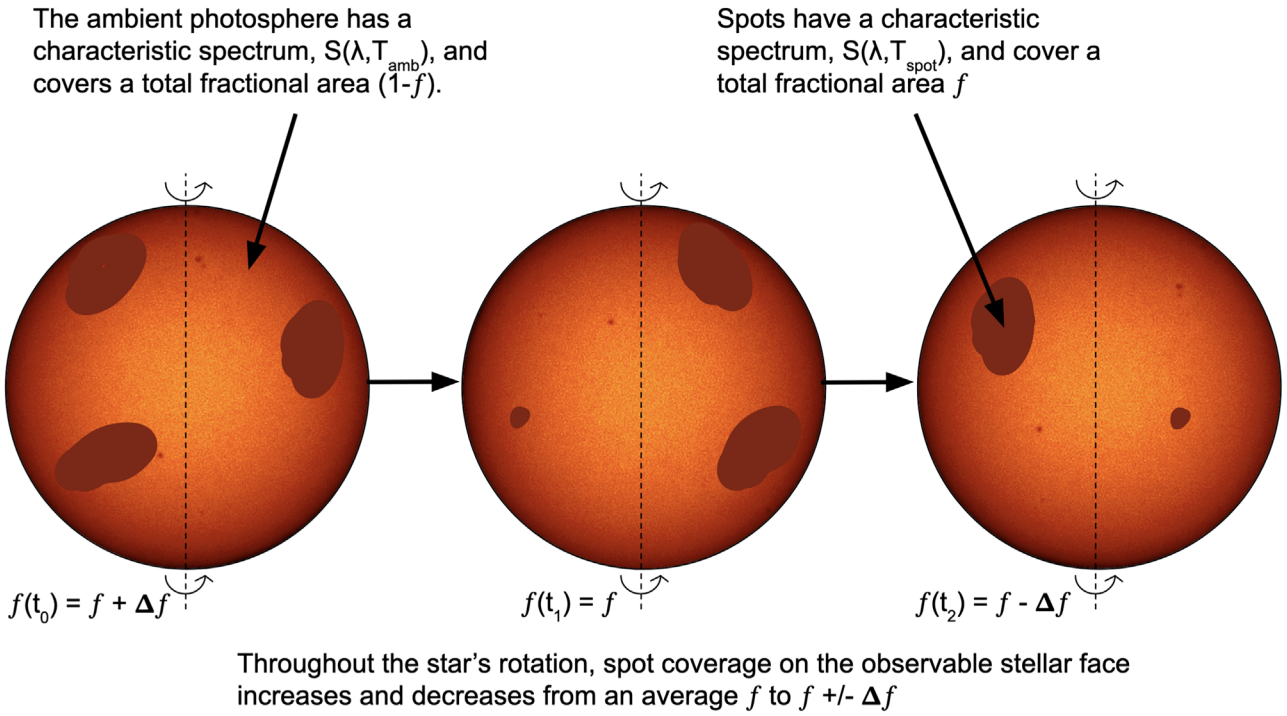

Figure 2. Cartoon of a spotted star showing the parameters used in this study.

Table 3
Priors Placed on Our Model Parameters in the Spot Characteristics Monte Carlo Simulation

Quantity	Prior
$T_{\rm eff}$ [K]	3650 ± 100
$T_{\rm hot}$ [K]	$\mathcal{U}[T_{\rm amb}, 12{,}000]$
$T_{\rm spot}$ [K]	$\mathcal{U}[2300, T_{\rm amb}]$
$T_{\rm amb}$ [K]	$\mathcal{U}[T_{\rm spot}, T_{\rm hot}]$
$f_{\rm hot}$	$\mathcal{U}[0,0.5]$
$f_{\rm spot}$	$\mathcal{U}[0, (1.0 - f_{\rm hot})]$
$\Delta f_{\rm spot}$	$\mathcal{U}[0, f_{\rm spot}]$

component (which may be faculae, flares, or something else) with temperature $T_{\rm hot}$, and $f_{\rm amb}$ is the coverage of the ambient photosphere which has temperature $T_{\rm amb}$. The ambient coverage is not a unique parameter in the model but is calculated as $f_{\rm amb} = 1 - (f_{\rm spot} + f_{\rm hot})$. This constraint effectively ensures that whatever combination of spectral components is being modeled accurately reproduces the known surface-averaged bolometric flux emitted from the stellar surface.

3.2.2. Photometric Variability

Following the formalism in Libby-Roberts et al. (2022), we can calculate the semiamplitude of variability due to spots as the following:

$$\frac{\Delta S(\lambda)}{S_{\rm avg}(\lambda)} = -\Delta f_{\rm spot}\left(\frac{1 - \frac{S(\lambda, T_{\rm spot})}{S(\lambda, T_{\rm amb})}}{1 - f_{\rm spot}\left[1 - \frac{S(\lambda, T_{\rm spot})}{S(\lambda, T_{\rm amb})}\right]}\right). \quad (4)$$

The expression above, the only calculation in our model which depends on $\Delta f_{\rm spot}$, is integrated across the filter bandpasses to generate a single variability datum for each filter. We account for the filter response curves by normalizing our variability integral by the filter response function:

$$\frac{\Delta S}{S_{\rm avg}} = \frac{\int_{\lambda_1}^{\lambda_2} \frac{\Delta S(\lambda)}{S_{\rm avg}(\lambda)} W(\lambda) S(\lambda, T_{\rm eff}) {\rm d}\lambda}{\int_{\lambda_1}^{\lambda_2} W(\lambda) S(\lambda, T_{\rm eff}) {\rm d}\lambda}, \quad (5)$$

where the SDSS filter response functions (W_λ) are acquired through `Speclite`.[11] The stellar spectrum term ($S(\lambda, T_{\rm eff})$, calculated at $T_{\rm eff} = 3650$ K), accounts for the nonuniform distribution of stellar flux emitted across the bandpasses. These bandpass-integrated model variabilities are then fit to the broadband variability measurements extracted from the stellar rotation curve models (Section 3.1).

We ignore a facular contribution to the rotational variability because magnetically active stars are expected to have photometric variabilities dominated by spots (Shapiro et al. 2016), but it factors into the calculation of $T_{\rm eff}$ and is still included as a flux component when we examine the photometric variabilities without the spectra. The variability light curve is also highly undersampled, so adding another component into the rotation model would be overfitting the very few (five) photometric variability data points we have.

3.2.3. Average Spectrum

From the NRES echelle spectra, we calculate a time-averaged spectrum which we model as a combination of a spotted spectrum and an ambient spectrum weighted by their globally averaged coverage:

$$S_{\rm avg} = f_{\rm spot} S(\lambda, T_{\rm spot}) + f_{\rm hot} S(\lambda, T_{\rm hot}) + f_{\rm amb} S(\lambda, T_{\rm amb}). \quad (6)$$

Older studies of starspots have been limited in this approach due to the computation time required to model thousands of spectral lines and as a result they typically probed specific regions and

[11] https://speclite.readthedocs.io/en/latest/filters.html

rotational or vibrational temperatures which may not be indicative of the bulk spot properties. Here we modeled as many possible regions of the spectrum as possible, including orders which have weak or nonexistent spot signatures as well as those with strong signatures indicative of very cool regions, to understand the most complete picture of the star provided by the spectral data.

3.3. Spot Contamination Model

Atmospheric absorption will induce a wavelength-dependent change in the transit depth ($\Delta D(\lambda)$) of the planet, expressed as:

$$\Delta D(\lambda) = \left(\frac{R_p}{R_*}\right)^2 + \Delta D(\lambda)_{\rm atm} + \Delta D(\lambda)_{\rm spot}, \quad (7)$$

with $\Delta D(\lambda)_{\rm atm}$ defined as:

$$\Delta D(\lambda)_{\rm atm} = \frac{2R_p}{R_*^2} H \times n(\lambda), \quad (8)$$

where H is the scale height and $n(\lambda)$ is the number of opaque scale heights at each wavelength, which typically varies between zero and five for cloud-free atmospheres (Seager et al. 2000).

Following the derivations in Rackham et al. (2018), Zhang et al. (2018), and Libby-Roberts et al. (2022), we can express $\Delta D(\lambda)_{\rm spot}$ as:

$$\Delta D(\lambda)_{\rm spot} = \left(\frac{R_p}{R_*}\right)^2 \left[\frac{(1 - f_{\rm spot,tra}) + f_{\rm spot,tra}\frac{S(\lambda, T_{\rm spot})}{S(\lambda, T_{\rm amb})}}{(1 - f_{\rm spot}) + f_{\rm spot}\frac{S(\lambda, T_{\rm spot})}{S(\lambda, T_{\rm amb})}} - 1\right]. \quad (9)$$

This expression can similarly be used to calculate the facular depth contribution but we assume this contribution is negligible on AU Mic. Equation (9) does not explicitly rely on $\Delta f_{\rm spot}$, but the value we derive for $\Delta f_{\rm spot}$ can be used to project the spot coverage at a given time or phase, which is needed to account for spot contamination at the time of transit. In this work we assume $f_{\rm tra}$ to be zero for both spots and faculae, which implies that the contamination calculated for a given set of parameters represents an upper limit relative to a spotted transit chord. Samples for $f_{\rm spot}$, $f_{\rm hot}$, $T_{\rm spot}$, $T_{\rm hot}$, and $T_{\rm amb}$ are injected into this model to generate a posterior distribution of $\Delta D(\lambda)_{\rm spot}$.

3.4. Experimental Design

We run several different iterations of the spot characteristics model in order to examine the information and constraints provided by each component of the data: we model the photometric measurements separately from the spectra, the spectra without photometric models, and the ensemble model which includes both data types. The model is set up as a Monte Carlo simulation using the `emcee` sampler (Foreman-Mackey et al. 2013), run with 100 walkers and 2000 steps with a 25% burn-in. Models ran past convergence in accordance with the autocorrelation time of the sampler chains (for a discussion of convergence and autocorrelation, see Foreman-Mackey et al. 2013). This framework maintains a distinction between the temperatures of the different spectral surface components ($T_{\rm spot} \leqslant T_{\rm amb} \leqslant T_{\rm hot}$) while allowing $f_{\rm spot}$ and $f_{\rm hot}$ to vary, enabling the models to arrive at solutions where the surface is $\geqslant$50% covered in spots. Technically $f_{\rm hot}$ is allowed to vary as high as 50% but in practice the models almost never preferred values of $f_{\rm hot}$ greater than a few percent. Time-domain analysis of the seven NRES spectra from F21 and 17 spectra from S22 should contain information about the change in spot coverage with stellar phase but no periodic signal could be found so we do not include a time-domain spectral model in the analysis. Independent modeling of the separate visits returned strongly consistent measurements for $f_{\rm spot}$, $f_{\rm hot}$, and $\Delta f_{\rm spot}$ which could be be a robust finding, considering the time between visits is 2× the 120–150 day activity evolution timescale (which we can approximate to be a spot decay timescale) measured by Donati et al. (2023).

4. Results

4.1. Variability Amplitude Results

For the F21 visit, we measure variability semiamplitudes, $\Delta S/S$, in g', r', and i' of 0.075 ± 0.006, 0.071 ± 0.006, and 0.041 ± 0.007, respectively, and for the S22 visit we measure $\Delta S/S$ of 0.075 ± 0.003 in g' and 0.075 ± 0.003 in r', shown in Figure 3 and summarized in Table 4.

Measuring the signal for i' was slightly challenging because, as the reddest bandpass, this filter showed the weakest variability signal and therefore the smallest S/N. Moreover, as AU Mic is much brighter than the nearby comparison stars and the exposure times are short, scintillation noise is prevalent. To account for poorly constrained measurements in i' and improve the internal consistency of our multicolor variability measurements, we impose a prior on the phase (θ) for i'. The independently modeled g' and r' rotation curves agree within their 1σ uncertainties in phase, so we use the average of their phases (1.91 ± 0.04) as a prior when modeling i', resulting in a modeled phase in agreement with g' and r'. This is a reasonable approach to improving our i' results because we would expect the phase of three separate but contemporaneous data sets to be equal, so forcing the i' phase to be consistent with g' and r' increases the consistency between the three measurements and lends confidence to the relative amplitudes our signal measurements. The phase is not used further in this work but will be useful for the analysis of AU Mic b's atmospheric transmission spectrum when we need to estimate the spot coverage at the time of transit.

4.2. Spot Characteristics Model

We examine the spot characteristics results when we model only the stellar effective temperature and photometric variability data (excluding the NRES spectral models) and similarly when we model only the NRES spectra with the stellar effective temperature (excluding the multicolor photometric variability data). Finally, we examine the results of modeling the stellar $T_{\rm eff}$, photometric variabilities, and NRES spectra together in an "ensemble" model which models the 12 spectral orders and multicolor variabilities for both visits, from which we report the final results.

4.2.1. Photometric Variability

Figure 4 shows our measured photometric variability semiamplitudes with random samples drawn from the photometry-only posterior distributions, with results listed in Table 5. The photometric variabilities, along with AU Mic' $T_{\rm eff}$, show evidence for essentially any spot coverage between 10% and 90% with temperature 3141^{+266}_{-389} K, changing throughout an orbit by $6\% \pm 3\%$. Solutions for ambient temperature are 3719^{+302}_{-502} K, with an upper limit of 40% coverage of a hot component with

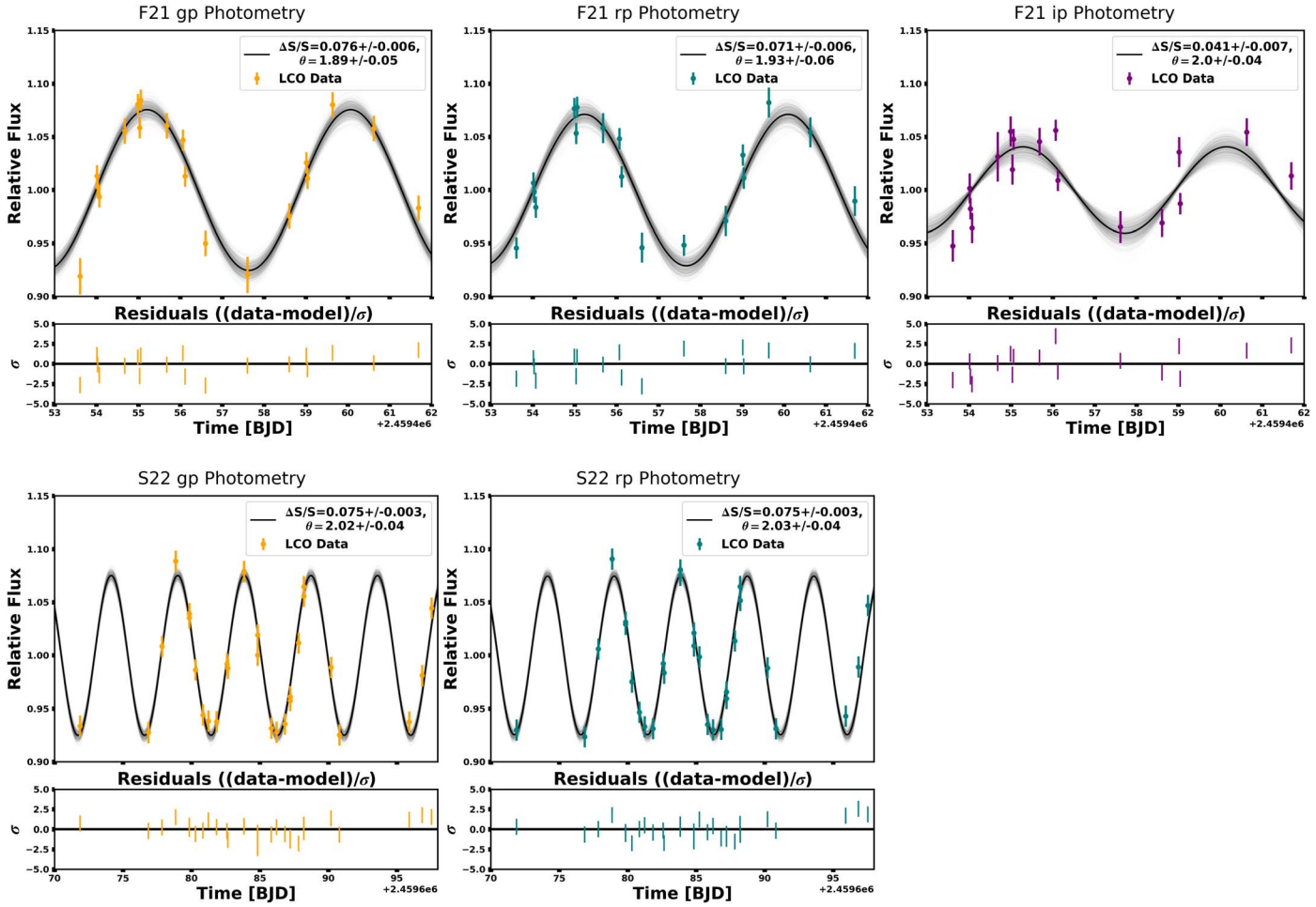

Figure 3. LCO 0.4 m photometry of AU Mic in the g', r', and i' filters with the rotation model fits described in Section 2. Variability decreases with wavelength, exhibiting a significant decrease between the r' and i' measurements. The shaded regions are randomly sampled models showing the distribution we quote as the uncertainty on the amplitude, and the color of each data set corresponds to the filter response curves in Figure 12. Model results are provided in Table 4.

Table 4
Parameters from the MCMC Fits of the Photometry

Filter	Amplitude	Phase
	First Visit (F21)	
g'	0.075 ± 0.006	1.89 ± 0.05
r'	0.071 ± 0.006	1.93 ± 0.05
i'	0.041 ± 0.007	2.00 ± 0.04
	Second Visit (S22)	
g'	0.075 ± 0.003	2.02 ± 0.04
r'	0.075 ± 0.003	2.03 ± 0.04

Note. The period was kept fixed at the literature period of 4.86 days while the phase and amplitude were modeled as a combination of sine and cosine terms.

temperature 4873^{+1922}_{-727}K. The hot component is only relevant to the effective temperature calculation in the variability-only modeling, so it is acting more as an extra free parameter to improve the fit than being related to anything physical. The measurement of $T_{\rm spot}$ is surprisingly consistent with results from the spectral models.

Two-temperature models of the variabilities return tighter constraints on the ratio of $T_{\rm spot}$ to $T_{\rm amb}$ and their individual measurements, but the measurement of $T_{\rm spot}$ is significantly warmer ($T_{\rm spot} = 3454^{+155}_{-208}$ K) than virtually every other measurement of $T_{\rm spot}$ we present in this paper. Measurements of $f_{\rm spot}$ and $\Delta f_{\rm spot}$ are consistent with the three-temperature fits. Results for the two-temperature modeling are in Table 6.

4.2.2. Spectral Decomposition Results

When modeling the 12 spectral orders (Figure 5) simultaneously and without photometric variability, we find more precisely constrained temperatures and coverages for all three components. The change in spot coverage, $\Delta f_{\rm spot}$ is unconstrained by these models because we are modeling time-averaged spectra. The stellar spectra indicate a large fraction ($f_{\rm spot} = 0.39 \pm 0.04$) of cool spots with temperature 2974^{+72}_{-71} K, a dominant "ambient" (warmer) photosphere with temperature 4002^{+14}_{-15} K, and a very tenuous detection of a hot component with temperature 8681^{+868}_{-629} K covering less than 0.5% of the surface.

Two-temperature models of the spectra result in fully consistent measurements of each parameter. The spot component measured to cover $41\% \pm 3\%$ of AU Mic has temperature 3083^{+31}_{-45} K, and the ambient photosphere temperature is measured to be 3998^{9}_{11} K.

4.2.3. Ensemble Model

Results from our ensemble model, where all five photometric variability measurements are jointly modeled with the spectra of both visits, are shown in Figures 6, 7, and 8, along with

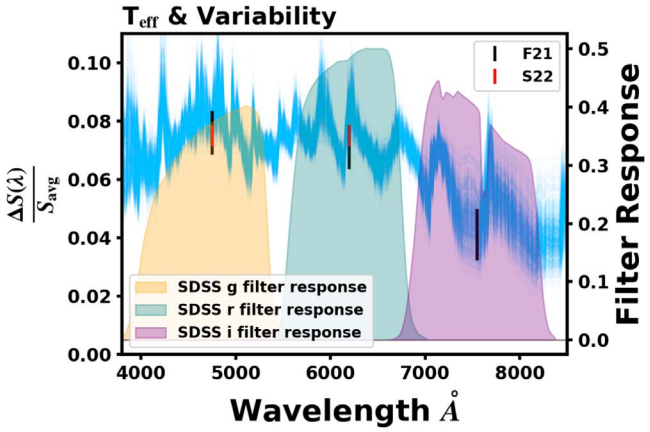

Figure 4. All five measured rotational variabilities with random models (blue) drawn from the variability model samples. The shaded regions in the background are the filter response curves for our observations. We fit both visits together because the photometric and spectroscopic data are consistent despite the 6 months between visits (e.g., Robertson et al. 2020). Variability decreases with wavelength as the spot-to-photosphere flux contrast decreases, and when modeling the visits separately we find that our solutions were very sensitive to the magnitude and uncertainty of the i' measurement. We have photometry for all three filters in F21 but only g' and r' in S22.

Table 5. This model finds well-constrained spot characteristics of $f_{\rm spot} = 0.39 \pm 0.04$, $\Delta f_{\rm spot} = 0.05^{+0.004}_{-0.003}$, $T_{\rm spot} = 3003^{+63}_{-71}$ K, and $T_{\rm amb} = 4003^{+15}_{-14}$ K. Similar results for the two-temperature modeling are shown in Table 6.

Some degenerate solutions can be seen which prefer what looks like a fourth flux component between 3600 and 3900 K with a coverage fraction of 6%–10%. This could be very weak evidence of the spot penumbra but attempts to extract that component were unsuccessful and can be pursued further in future work.

We can see that this ensemble model exhibits characteristics of both the photometry-only and spectra-only models. The photometric variabilities strongly constrain $\Delta f_{\rm spot}$ and limit how cool the spots can be but provide poor constraints on the coverage fraction of spots. Variability measurements in multiple wave bands across the optical–near-infrared (NIR) constrain the temperature contrast because the relative change in variability with wavelength is set by the ratio of spectral components. Further into the red, the spot and ambient spectra are more similar and the variability is less. At bluer wavelengths, there is an increasing contrast between cool spots and the surrounding photosphere, up to a maximum of 100% (where the spot flux is effectively 0 relative to the surrounding photosphere).

The spectral decomposition returns a precise estimate of $f_{\rm spot}$, which is further constrained with the inclusion of photometric modeling. The cold spot preference of the spectral models is balanced by the photometric limits on how cool the spots can be, given the contrast at longer wavelengths. The spot coverage fraction is unconstrained when modeling the photometry due to degenerate observational effects between $f_{\rm spot}$ and $T_{\rm spot}$, but is precisely constrained when spectral modeling is included. The ensemble model results are primarily driven by the spectra, with the photometry being most important for the measurement of $\Delta f_{\rm spot}$.

We argue that the consistency between measurements of the separate components based on different data–model combinations indicates that the results we report from the ensemble model are physically realistic.

The two-temperature models agree with the three-temperature results remarkably well, showing a spot coverage of $41\% \pm 3\%$ that changes throughout a rotation by $5.1\% \pm 0.3\%$, with $T_{\rm spot} = 3093^{+29}_{-41}$ and $T_{\rm amb} = 3998^{+10}_{-12}$.

4.3. Spot Contamination

We forward modeled spot contamination (Equation (9)) under the assumption of 0% spot coverage on the transit chord using the ensemble model posteriors generated in the previous step, as shown in Figure 9. At short wavelengths like the TESS bandpass (0.6–1 μm), contamination ranges from 550 to 1400 ppm. In the WFC3 bandpass, contamination is between 500 and 750 ppm, and decreases to 250–500 ppm at longer wavelengths. The transit depth of AU Mic b reported in Szabó et al. (2022) calculated from TESS and CHEOPS (0.33–1.1 μm) transits translates to about 1875 ppm, so the spot contamination is 25%–75% of that signal if $f_{\rm tra} = 0$. This means that without accounting for spot contamination, AU Mic b's true radius (3.46 $R_{\rm E}$ if the Szabó et al. 2022 value is uncontaminated) may be overestimated by as much as 0.5–1.7 Earth radii. For AU Mic c, the Szabó et al. (2022) depth is about 980 ppm, with contamination calculated to be between 400 and 750 ppm. This translates to an overestimated planetary radius of between 0.6 and 1.3 Earth radii.

The magnitude of this shorter-wavelength contamination may be much different at different points in AU Mic's activity cycle and long-term magnetic evolution, so these are rough estimates and contemporaneous measurements of transit depths across the optical to infrared would shed more light on the true radius of AU Mic b.

5. Discussion

In this work, we present an analysis of broadband photometry and high-resolution spectroscopy to constrain the spot characteristics on AU Mic. Studying spots is a necessary first step in addressing spot contamination in the HST/WFC3 transmission spectrum of AU Mic b and subsequently understanding its atmosphere. Using the stellar effective temperature, multicolor time-series photometry, and high-resolution stellar spectra, we parameterized the spectroscopic and photometric effects of starspots into spot coverage and temperature, with a well-constrained ambient temperature and tentative measurement of a hot component.

5.1. The Photometric Variability Spectrum

Photometric variability has a wavelength-dependent characteristic which can be used to constrain the primary flux components. Amplitudes increase to some maximum at blue wavelengths as the flux contrast increases to one, and decreases at redder wavelengths toward the Rayleigh–Jeans limit. The shape and extent of the amplitude of rotational variability as a function of wavelength provides an important constraint on spot temperatures. Because our measured variability amplitudes are significantly less in i' than g' or r', the spot temperature contrast is very sensitive to the magnitude and uncertainty of i'. The i' variability measurement thus carries more weight than any other single data point in this study, as it strongly constrains the spot contrast and limits how cool the spots can be. If the i' measurements showed greater variability, this would allow the spot temperature solutions to be cooler, as the contrast would be greater into the red. The variability must instead decrease in this bandpass, which forces the range of solutions to be narrower and the spot contrast to be within a certain range. The importance of this i' measurement indicates that further

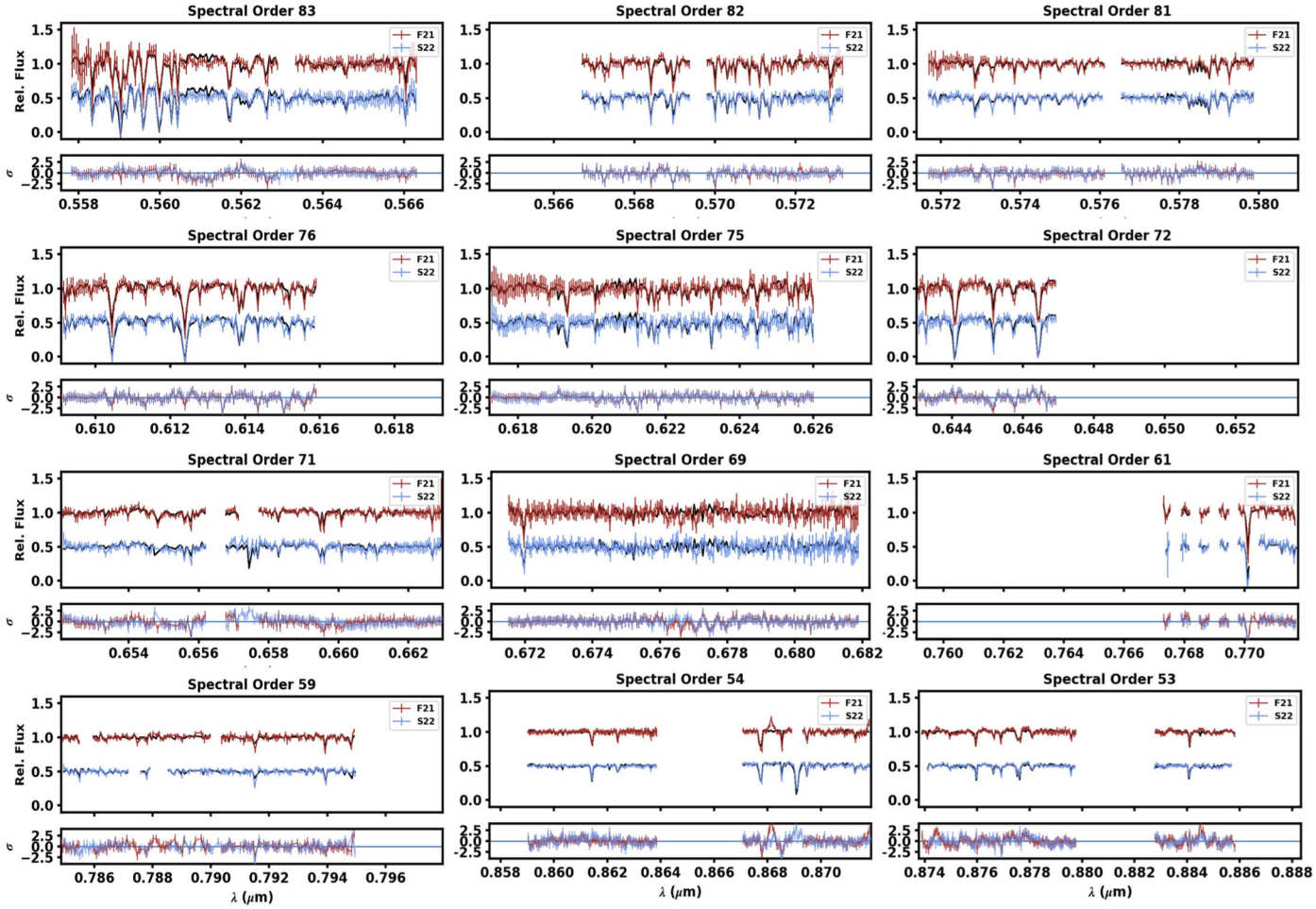

Figure 5. Spectra used in this analysis. The red and blue data points (F21 and S22, respectively) are median averaged in time and have had their uncertainties normalized so a 3650 K template model has a reduced χ^2 of 1. A total of 100 randomly sampled models are plotted in black, which in most cases have a tight spread and are difficult to notice in these plots. Despite some poorly fit line depths, there is a tight constraint on the spot temperatures and filling factors from the spectra with or without photometric variabilities.

photometric studies of spotted stars must be sure to include multiple bandpasses in the optical–infrared in order to determine precisely the wavelength regime where variability decreases or "turn-off" happens. The wavelengths where this turn-off is observed are highly descriptive of the stellar spot spectra.

5.2. Two Flux Components or Three?

The primary results in this work are reported from the three-temperature modeling, but we examine how those results changed when modeled with only two temperatures, finding it returns measurements for $f_{\rm spot}$, $\Delta f_{\rm spot}$, $T_{\rm spot}$, and $T_{\rm amb}$that are strongly consistent with the three-temperature results. When we allow a third component, it finds a poorly constrained temperature between 7000 and 10,000 K, with a small number of solutions closer to the ambient photosphere, around 4000–5000 K. If the 7000–10,000 K component is physical, it is likely a flux contribution from flares, which occur so frequently they cannot entirely be removed by time averaging.

Faculae on M dwarfs may be up to a few hundred kelvin above the ambient photosphere (e.g., Norris et al. 2023) and a small cluster of solutions in this temperature range stand apart from the primary results (seen in Figures 6 and 7). This could be indicative of faculae but we did not recover that component in concerted attempts and its filling factor must be even less than the filling factor measured for the hotter temperature, measured to be less than 0.5%.

There is one key difference in the outcomes of the two- and three-temperature models. When modeling only $T_{\rm eff}$ and photometric variabilities, the two-temperature model returns a significantly warmer $T_{\rm spot}$ and a tighter ratio of $T_{\rm spot}$ to $T_{\rm amb}$ compared with the three-temperature model. A third temperature, which only factors into the calculation of $T_{\rm eff}$, brings the spot temperature solutions into agreement with the other measurements we report, with larger uncertainties and a weaker (though still noticeable) relationship between the spotted and unspotted temperatures.

Further investigation into multicolor rotation models and independent measurements of spot temperatures will be needed to help clarify when two- or three-temperature rotation models are most appropriate, and what cautions to impose on interpreting spot characteristics from photometric variabilities alone.

5.3. Physical Interpretation of AU Mic's Spot Characteristics

Much work has been done to measure and theoretically determine the spot temperatures, distributions, and filling factors as a function of stellar type. Still, observational evidence of consistent spot temperatures and precise filling factors for AU Mic is tenuous. Spot characteristics are notoriously difficult to determine and different approaches can lead to inconsistent results. Here we will discuss the results,

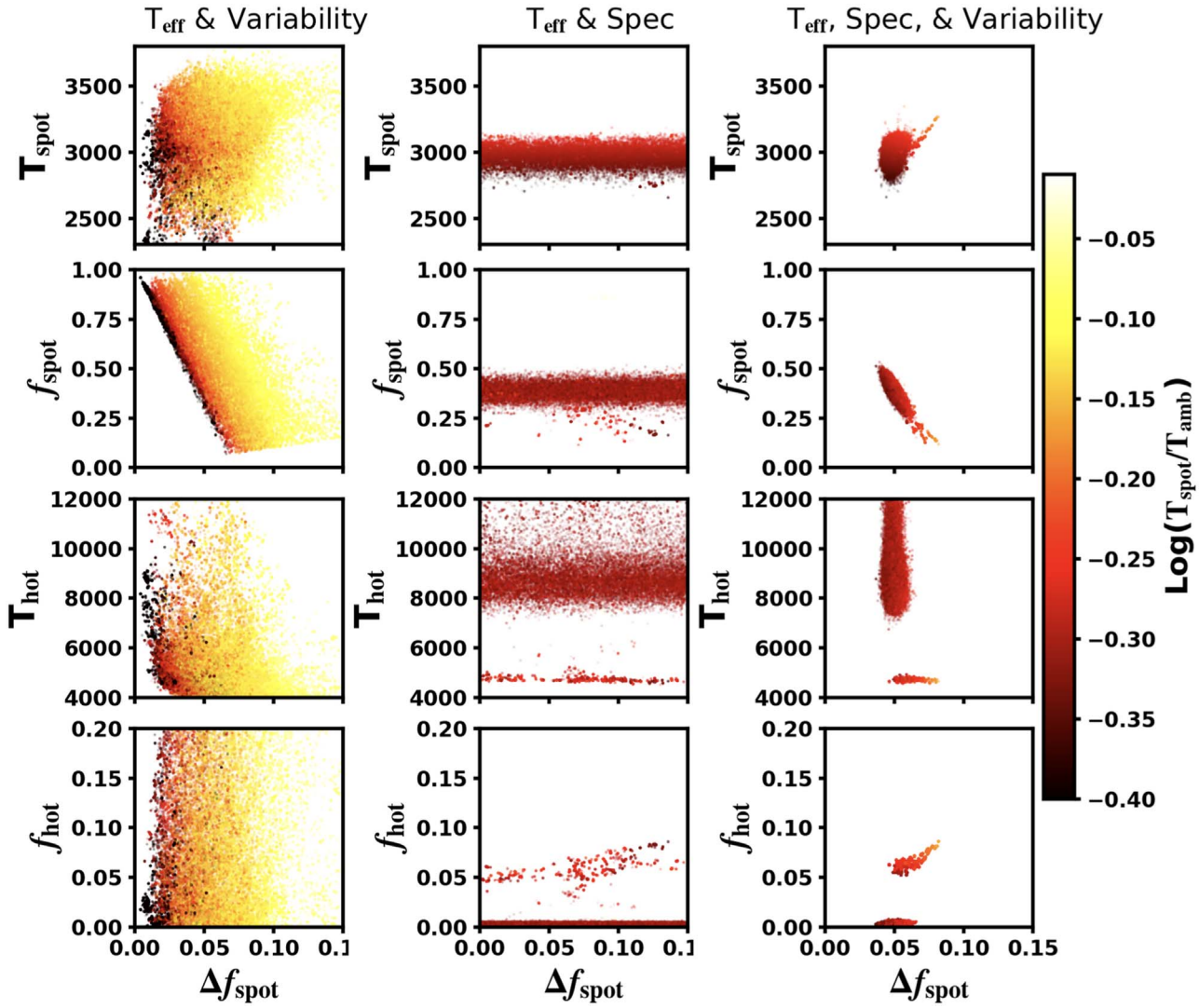

Figure 6. Posterior samples for the variability model (left), spectral model (middle), and the ensemble model (right), which retains characteristics of the separate model results. The spectra constrain how hot the spot temperatures can be while the photometry constrains how cool they can be. Limits on the spot coverage fraction are mostly provided by the spectral modeling, with the variability providing constraints on $\Delta f_{\rm spot}$. The color of each point corresponds to the logarithm of the temperature ratio ($T_{\rm spot}/T_{\rm amb}$), with redder points being spots that are further from the ambient temperature.

limitations of this approach, and physical interpretation of AU Mic's starspots.

5.3.1. Spot Temperature

We report a characteristic spot temperature for AU Mic of $T_{\rm spot} = 3003^{+63}_{-71}$ K. A study of diatomic molecular lines in AU Mic's spot spectra found in Berdyugina et al. (2011) implies a ΔT ($T_{\rm eff} - T_{\rm spot}$) of 500–700 K, which would translate to spot temperatures of 3000–3200 K for a star with a $T_{\rm eff}$ of 3700 K. More recently, Ikuta et al. (2023) calculate $T_{\rm spot} = 3140 \pm 64$ K for AU Mic based on Equation (4) of Herbst et al. (2021), which is based on the work done by Berdyugina (2005). Rackham et al. (2018) suggest that for cool stars, $T_{\rm spot}$ can be estimated as $0.86 \times T_{\rm phot}$ (which we have labeled $T_{\rm amb}$ in this work). Given our modeled $T_{\rm amb}$ of 4003^{+15}_{-14} K, the estimated spot temperature would be roughly 3300–3400 K, which is over 200 K warmer than our spectral and ensemble results but in agreement with our photometry-only model results. Recent work by Flagg et al. (2022) found evidence of a cold H_2 layer in AU Mic's photosphere with $1000\ {\rm K} < T_{\rm spot} < 2400$ K. Afram & Berdyugina (2019) use molecular lines to measure spot temperatures and find that M0 stars may have spot temperatures ~2200 K less than the stellar effective temperature, implying the spots on AU Mic may have $T_{\rm spot} \lesssim 1500$ K and $T_{\rm spot}$-to-$T_{\rm eff}$ ratios roughly $\leqslant 0.4$.

Placed in context, the spot temperatures we measure in this work are much cooler than the $\Delta T = 400$ K or $T_{\rm spot} = 0.86\, T_{\rm amb}$ estimates for low-mass stars and slightly cooler than (but consistent with) the Ikuta et al. (2023) and Berdyugina et al. (2011) estimates for AU Mic, warmer than some of the molecular and vibrational estimates for spots, but consistent with older measurements of spot temperatures on young active stars similar to AU Mic (e.g., Ramsey 1980; Vogt 1981). The range of temperatures measured using different methods is likely due to a combination observational degeneracy, incorrect assumptions about spot physics, and different methods being diagnostic of different regions of a spot. If the spots on AU Mic have observably complex temperature profiles and extensive penumbrae, then the $f_{\rm spot}$ recovered in these models may be an overestimate of the true spot umbra and an underestimate of the spot umbra + penumbra.

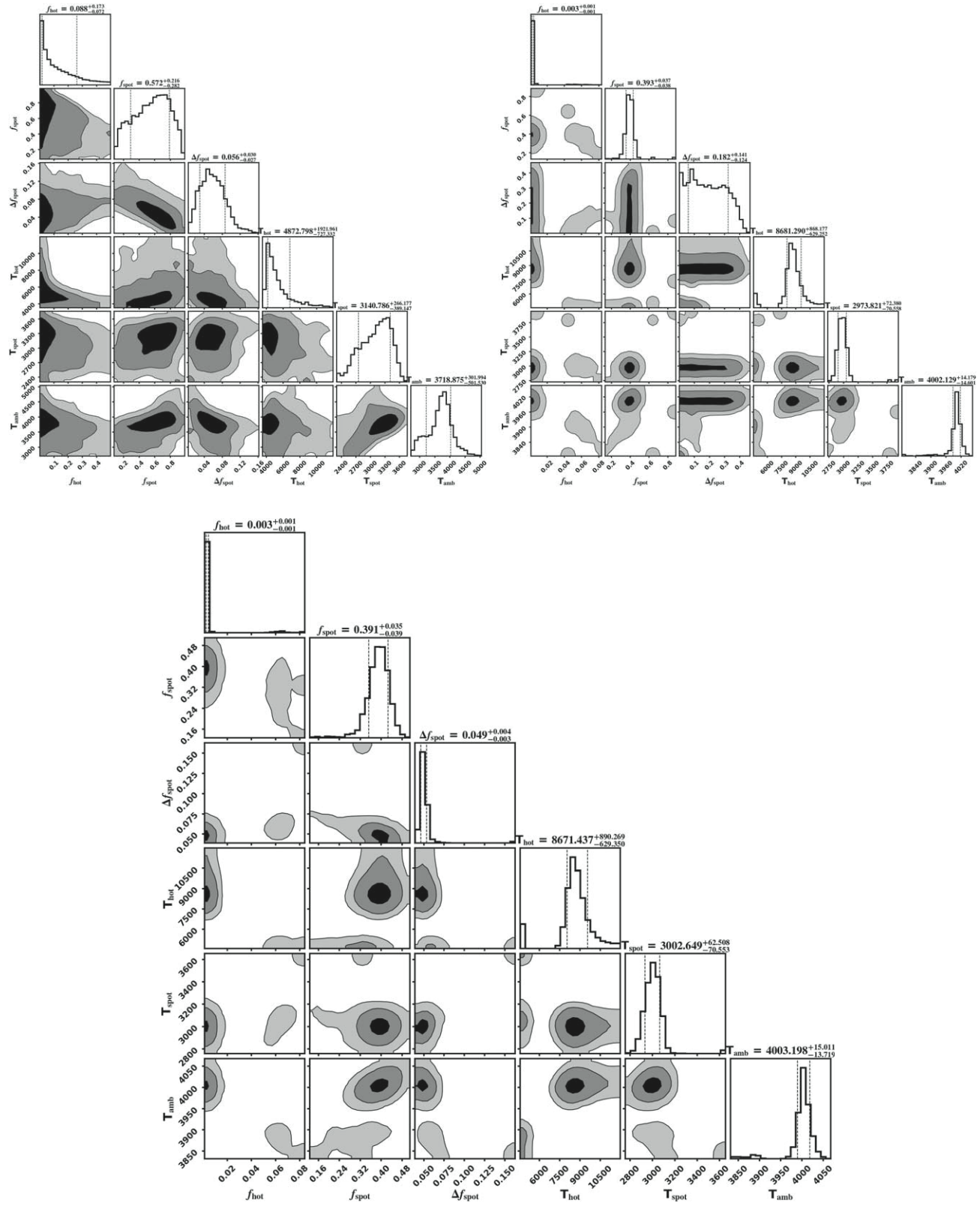

Figure 7. Posterior histograms for the variability (top left) and spectral models (top right), with the ensemble results (bottom) exhibiting what look like the separate model posteriors multiplied together.

5.3.2. Spot Filling Factor

Our models indicate that the spot filling factor for AU Mic is $f_{\rm spot} = 0.39 \pm 0.04$, with a change in spot coverage throughout a stellar rotation of $\Delta f_{\rm spot} = 0.05^{+0.004}_{-0.003}$. This estimate is within the very broad and uncertain range of possible spot coverage fractions measured for Sun-like and cooler stars and indicates a heavily spotted stellar surface. Yamashita et al. (2022) estimate an $f_{\rm spot}$ of between 1% and 21% for zero-age main-sequence

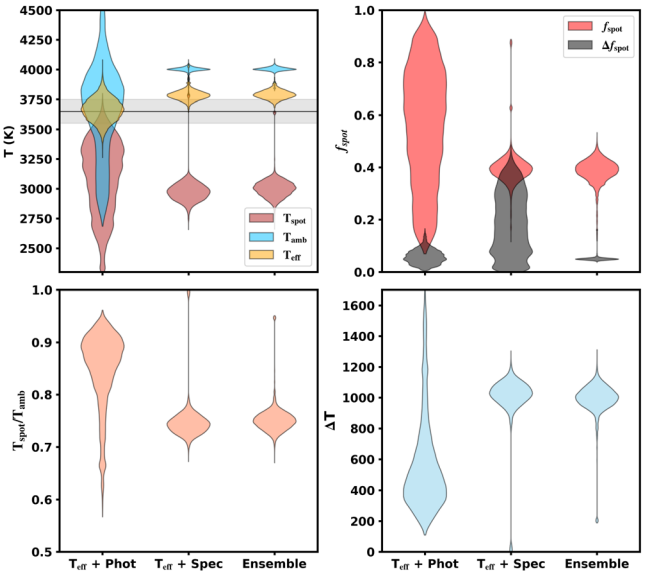

Figure 8. Violin plot posteriors for the variability modeling (left distribution on each panel), spectral modeling (middle distribution), and the ensemble model (right distribution). Top left: temperature posteriors showing T_{spot}, T_{amb}, and T_{eff}. Top right: f_{spot} and Δf_{spot} posteriors. Bottom left: temperature ratio, T_{spot}/T_{amb}. Bottom right: ΔT, the difference between the spotted and ambient temperatures. The ensemble results exhibit a narrower parameter space for spot characteristics, which is effectively the product of the variability and spectral posteriors.

Table 5
Parameters from Fitting the Different Data Combinations with a Three-temperature Model

Parameter	Photometry Model	Spectral Model	Ensemble Model
T_{spot} (K)	3141^{+266}_{-389}	2974^{+72}_{-71}	3003^{+63}_{-71}
f_{spot}	$0.57^{+0.22}_{-0.28}$	0.39 ± 0.04	0.39 ± 0.04
Δf_{spot}	0.06 ± 0.03	<0.40	$0.05^{+0.004}_{-0.003}$
f_{hot}	<0.40	<0.01	<0.005
T_{hot} (K)	4873^{+1922}_{-727}	8681^{+868}_{-629}	8671^{+890}_{-629}
T_{amb} (K)	3719^{+302}_{-502}	4002^{+14}_{-15}	4003^{+15}_{-14}
T_{eff} (K)	3664 ± 101	3783 ± 37	3789 ± 35
χ^2	2.59 (2.59)	2124 (0.581)	2136 (0.584)

Note. The photometry model uses the 5 photometric variability measurements and the spectral model uses 12 spectral orders from both visits. The ensemble model is applied to all the photometric and spectroscopic data. Results are broadly consistent with the two-temperature model, most importantly recovering an approximately 3000 K spot in either case. The results we recommend citing for AU Mic's surface components are the ensemble model results in the rightmost column of this table.

stars using a fixed starspot temperature variability model, but such models are typically underestimates on f_{spot} (Apai et al. 2018; Rackham et al. 2018). Cao et al. (2022) use APOGEE *H*-band spectra to measure average spot filling factors to be 0.248 ± 0.005 for active stars in the Pleiades cluster and 0.03 ± 0.008 for main-sequence G and K stars in M67. Other estimates of f_{spot} for low-mass stars range from <1% to 50% (see Table 3 in Rackham et al. 2018). Our results are consistent with the range of expected coverage fractions, and our derived Δf_{spot} is consistent with the values modeled by Libby-Roberts et al. (2022) of $\Delta f_{spot} \leqslant 0.1$, though this is for a much older and slowly rotating star.

Table 6
Parameters from Fitting the Different Data Combinations with a Two-temperature Model

Parameter	Photometry Model	Spectral Model	Ensemble Model
T_{spot} (K)	3454^{+155}_{-208}	3083^{+31}_{-45}	3093^{+29}_{-41}
f_{spot}	$0.61^{+0.22}_{-0.27}$	0.41 ± 0.03	0.41 ± 0.03
Δf_{spot}	$0.08^{+0.06}_{-0.04}$	<0.4	0.05 ± 0.003
T_{amb} (K)	3876^{+234}_{-157}	3998^{9}_{11}	3998^{+10}_{-12}
T_{eff} (K)	3649 ± 98	3704 ± 24	3707 ± 24
χ^2	1.9 (1.9)	3060 (0.837)	3058 (0.836)

Note. The photometry model uses the 5 photometric variability measurements and the spectral model uses 12 spectral orders from both visits. The ensemble model is applied to all the photometric and spectroscopic data. The primary difference compared to the three-temperature results can be seen in the temperatures measured for T_{spot} and T_{amb}.

5.4. Caveats

Here we will briefly describe some of the limitations of this work and possible directions for future spot studies.

1. We use a simple sinusoidal rotation model, which is not necessarily the best choice for complex rotation curves like AU Mic's, but the photometry is not densely sampled and individual measurements have large uncertainties, so for the primary purpose of measuring the relative amplitude of variability between filters we argue this is an appropriate model.
2. AU Mic is a bright star, so ground-based differential photometry is difficult with LCO's field of view. Without similarly bright field stars, our photometry is very noisy, limiting the precision with which we can measure variability signals, especially in redder bandpasses.
3. Our spot contamination forward models assume that $f_{tra} = 0$, which means our contamination results are upper-limit cases for different sets of spot parameters. In reality, there may be some nonzero fraction of spot coverage on the transit chord, which will lower the contamination level in the transmission spectrum.
4. It is unclear what the source of the hot component is or whether it is truly a real signal, and the choice to include a third component affects the measurement of the spot temperature from photometric variability models.
5. Our understanding of M-star photosphere spectra is limited with the current generation of high-resolution synthetic spectral libraries like the Husser et al. (2013) PHOENIX models, described in detail by Iyer & Line (2020) and Rackham & de Wit (2023). Choosing the best spectral template is a problem for cool stars generally, but describing AU Mic with these models is further complicated by its pre-main-sequence age, a specific environment for which no truly appropriate model spectra yet exist. Alternative spectral models for M dwarfs exist, such as BT-SETTL (Allard 2014) or SPHINX (Iyer et al. 2023), but those are low- to mid-resolution libraries whereas the Husser et al. (2013) library has a resolution of $R = 100{,}000$–$500{,}000$ and is more appropriate for the $R = 53{,}000$ echelle spectra we acquired.

6. Conclusions

In this work, we have demonstrated the use in acquiring broadband photometry and high-resolution spectroscopy of

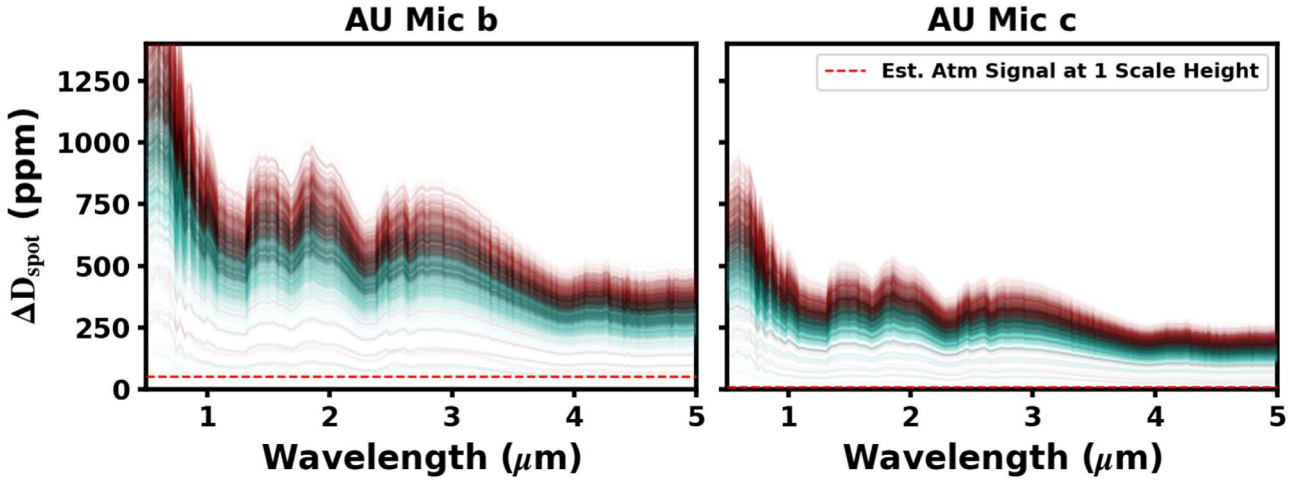

Figure 9. Forward-modeled spot contamination in the transmission spectra of AU Mic b (left) and AU Mic c (right) with models calculated using the sampled parameters from the ensemble model posterior. Red corresponds to models with $f = f_{spot} + \Delta f_{spot}$ (the point of maximum spot coverage and minimum flux throughout AU Mic's rotation), black to $f = f_{spot}$, and turquoise to models with $f = f_{spot} - \Delta f_{spot}$. Atmospheric depth estimates come from Equation (8) and are calculated to be 52 ppm for AU Mic b and 10 ppm for AU Mic c at one scale height. For an optimistic case where we can measure five scale heights in a cloud-free atmosphere, AU Mic b's atmospheric features will be comparable to lower estimates of spot contamination, while AU Mic c's atmospheric features will still be a factor of a few below the lowest contamination scenarios.

only the star (without data acquired during transit) for the purpose of studying starspots and estimating their effect on transmission spectra. The results of our modeling lead us to the following conclusions:

1. At the time of these observations, AU Mic may have been $f_{spot} = 39\% \pm 4\%$ covered in spots with a change of $\Delta f_{spot} = 6\% \pm 1\%$ throughout a rotation. The spots have a bulk (flux weighted, not distinguishing umbra from penumbra) temperature of $T_{spot} = 3003^{+63}_{-71}$ K surrounded by a $T_{amb} = 4003^{+15}_{-14}$ K photosphere. We found very weak evidence for facular coverage, and tentatively detect evidence of flux from flares with characteristic temperature 8671^{+890}_{-629} K. The fractional uncertainties measured on our final results for T_{amb} and T_{spot} come out to 0.25% and 2%, respectively. Berardo et al. (2023) report theoretical precision limits on stellar spectral models with current instruments and spectral libraries, finding we can constrain photospheric spectra to $\geqslant$0.2% and spot spectra down to 1%–5%, which translate to temperature uncertainties of $\geqslant$0.05% on T_{amb} and 0.25%–1.25% on T_{spot}.
2. Spot contamination in the transmission spectra of AU Mic b will be significant, adding between 250 and 1200 ppm contamination across the 0.5–5 μm range, overlapping with wavelengths where we expect planetary absorption features. This contamination is based on zero spot coverage on the transit chord, which could likely be an incorrect assumption if the large spot coverage fraction we measure is accurate. Nevertheless, spot contamination may be causing us to overestimate significantly the radii of AU Mic b and c. Determining the true planetary radii may require further acquisition and study of contemporaneous multicolor transit observations.
3. From these measurements we calculate $T_{amb} - T_{spot} = 1000$ K and $T_{spot}/T_{amb} = 0.75$. Spots this cool should show up noticeably if occulted in transit if our measurements and interpretation of AU Mic's photosphere are correct, but none have yet been confirmed. With AU Mic's short period and large radius, it is possible that spots exist primarily or only at high latitudes, in which case spot crossings would be rarely or never observed.
4. For stellar surfaces dominated by a single heterogeneity like spots (or faculae, but the picture becomes more complicated with significant filling factors of both), multicolor photometric variabilities provide significant constraints on the ratio of T_{spot}/T_{amb} (or T_{fac}/T_{amb}) and potentially accurate measurements of T_{spot}. Sampling the sensitive regions of a star's variability spectrum, even with broad photometric bandpasses, is useful for roughly estimating the temperatures of different spectral components.
5. Modeling the data with either two- or three-temperature spectral decomposition did not significantly change the measurements of T_{spot}, T_{amb}, or Δf_{spot}, which indicates that these measurements are robust. As we are uncertain of the nature and significance of the hot component we detect, further investigation of the phase-resolved stellar spectrum may help distinguish the nature of the different flux components.
6. Modeling only the variabilities provided a less accurate result for the coverage fraction when only two temperatures are allowed, even though this only affects the calculation of T_{eff}. The three-temperature T_{eff} and variability model returns an accurate (but highly uncertain) spot temperature while the two-temperature T_{eff} and variability model prefers spots closer in temperature to the photosphere. We recommend further investigation into the accuracy of measuring spot and/or facula temperatures with multicolor rotation modulations allowing both two and three temperatures.
7. Improving measurements of spot characteristics on exoplanet host stars and understanding spot contamination is challenging but tractable with a multimodal approach that covers a broad range of the visible–IR electromagnetic spectrum. As spot models and synthetic

spectra improve, spot characteristics on our host stars will become much clearer.

Acknowledgments

The authors thank the anonymous referee for the timely, thorough, and encouraging review that led to significant improvements to the manuscript. This material is based upon work supported by the National Science Foundation Graduate Research Fellowship Program under grant No. DGE-1650115. Any opinions, findings, and conclusions or recommendations expressed in this material are those of the authors and do not necessarily reflect the views of the National Science Foundation. This work makes use of observations from the LCOGT network. W.W. thanks Jessica Libby-Roberts, Hannalore Gerling-Dunsmore, Dennis Tilipman, Girish Duvuuri, Ward Howard, John Monnier, Steve Cranmer, Gibor Basri, and Steve Vogt for conversations that helped aspects of this project. W. W. and Z.K.B.T. were supported through STScI grant HST-GO-15788 and the NSF CAREER program (AST-1945633). A.W.M. was supported by grants from the NSF CAREER program (AST-2143763) and NASA's exoplanet research program (XRP 80NSSC21K0393). E.R.N. was supported by HST-GO-15836.

Software: The Python code used in this paper is available on the author's GitHub (https://github.com/will-waalkes/AUMicTLSE). This project made use of many publicly available tools and packages for which the authors are immensely grateful. In addition to the software cited throughout the paper, we also used `Astropy` (Astropy Collaboration et al. 2013, 2018, 2022), `NumPy` (van der Walt et al. 2011), `Matplotlib` (Hunter 2007), `Pandas` (The pandas development team 2024), and Anaconda's `JupyterLab`.

Appendix

We include this appendix to show some of the spectral data (Figures 10 and 11), visit-specific models of the photometric variabilities (Figure 12), and order-specific modeling of the NRES spectra (Figure 13). Comparing the F21 and S22 variability models demonstrates how important the i' measurement is and the relative constraints provided with or without it. The order-specific spectral models show agreement in many ways, as well as some poorly constrained orders which are likely due to telluric contamination.

Figures 10 and 11 show spectral order 53 from both visits as examples of how the data looked before and after being processed and the full figure sets can be found in the online journal, including orders that were cut from final analysis.

Appendix A
Visit-specific Variability Measurements

While the magnitude of stellar variability in any given wave band is related to degeneracies between spot temperature and spot coverage, the relative variability between photometric bandpasses and the wavelengths where the variability begins to decrease contain a lot of information about the spectral temperatures on the surface of the star. If the bulk spot temperatures are very cold relative to the photosphere, the

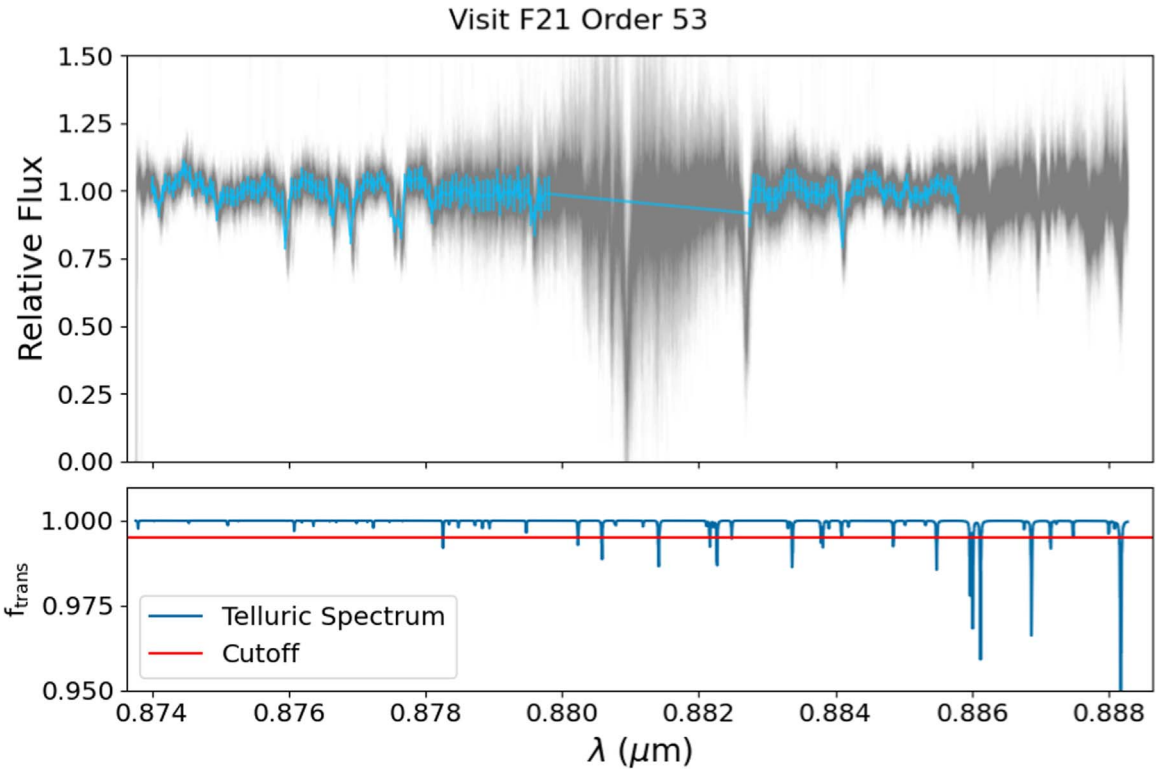

Figure 10. Order 53 from visit F21 with the spectral orders used in this analysis extending from order 53 (0.881 μm) to order 83 (0.562 μm). Stacked in gray are individual spectra collected from 2021 August 24 to 2021 September 9. In blue is a single spectrum derived from the time-series observations, which have been binned to 0.05 nm, telluric corrected, median averaged in time, and continuum normalized.

(The complete figure set (31 images) is available.)

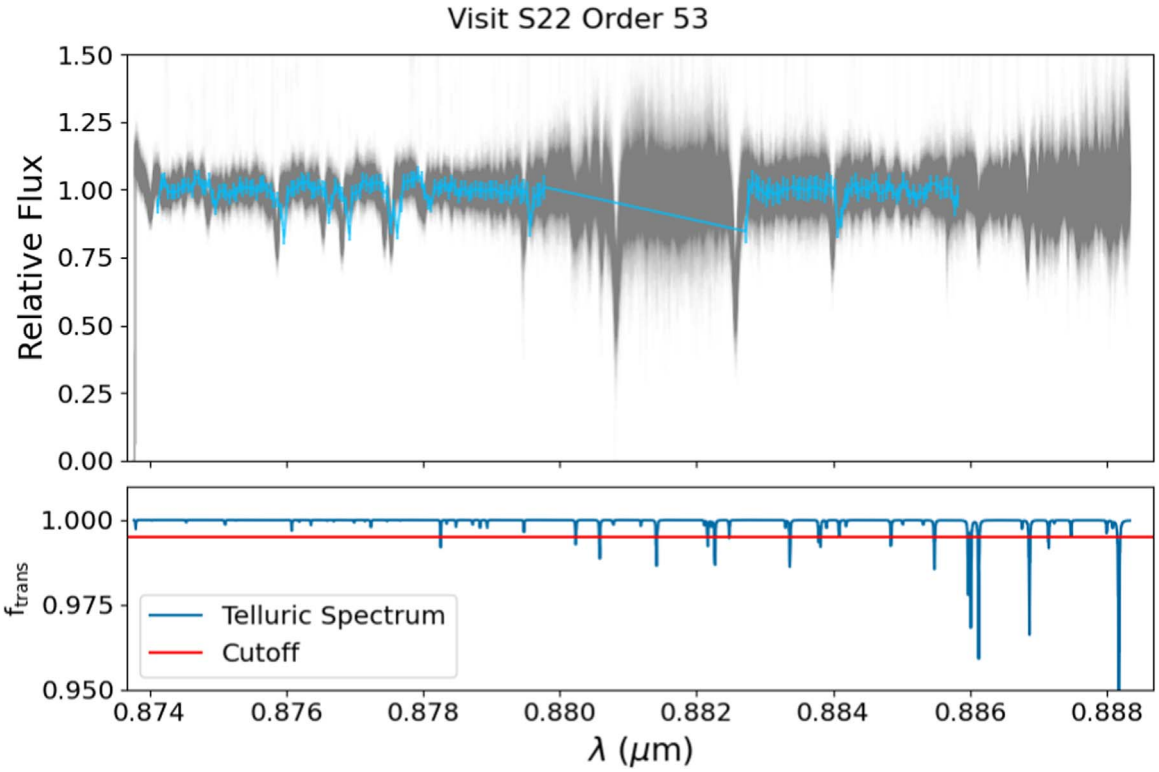

Figure 11. Order 53 from visit S22 with the spectral orders used in this analysis extending from order 53 (0.881 μm) to order 83 (0.562 μm). Stacked in gray are individual spectra collected from 2022 April 2 to 2022 April 17. In blue is a single spectrum derived from the time-series observations, which have been binned to 0.05 nm, telluric corrected, median averaged in time, and continuum normalized.

(The complete figure set (31 images) is available.)

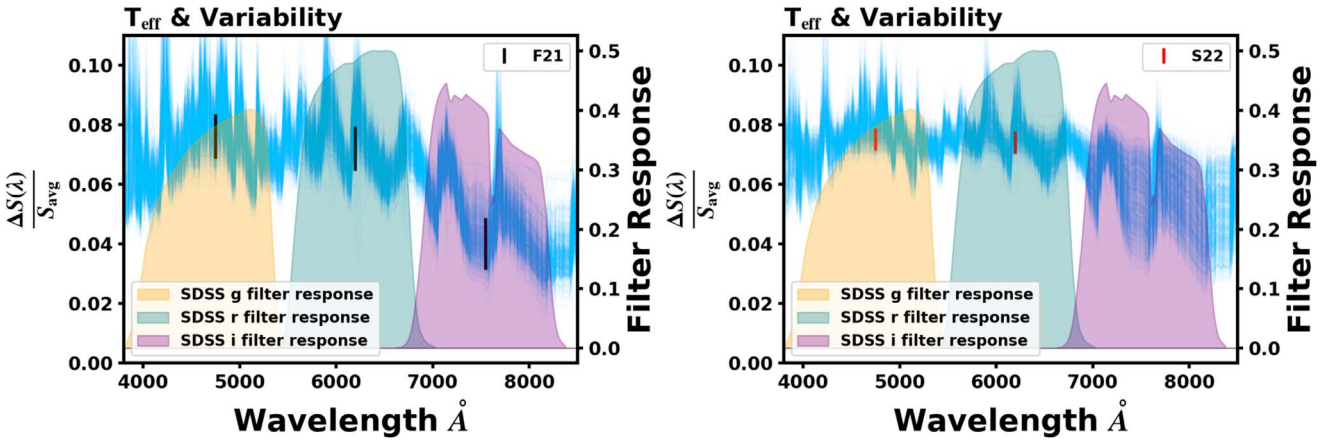

Figure 12. F21 (left) and S22 (right) sampled variability models (without spectral fits). The tighter model constraints imposed by an i' measurement can be seen in the spread of model solutions in the red when comparing visits. The presence or absence of i' is strongly constraining and further work should emphasize multiband measurements to constrain the spectral temperature contrast better.

variability will remain high at redder wavelengths. Similarly, if spot temperatures are closer to the ambient photosphere temperature, then the variability will decrease within optical and bluer wavelengths. The right panel in Figure 12 shows the greater spread in models at redder wavelengths resulting from the absence of an i' measurement, allowing the spot temperatures to be much cooler and much further from the ambient photosphere. The different model solutions possible are strongly constrained by this i' variability, and we extend that observation to say that multicolor photometric variabilities covering the optical–NIR provide very strong constraints on the temperature contrast for spotted stars.

Appendix B
Spectral Decomposition by Order

In the ensemble model described in the main text, we fit spotted spectral models to 18 orders simultaneously, but here we examine the results from modeling each order individually to check for consistency between orders and which orders might be the most informative. In this part of

the modeling, we model the data from both F21 and S22 with the same set of parameters, under the assumption that AU Mic's spot characteristics have not changed measurably between visits. Examining the results (Figure 13), we cut orders from the analysis if their solutions are poorly constrained and they satisfy any of the following criteria: there is telluric contamination, unconstrained ambient characteristics (which should be the dominant signal), or extremely cold spot temperatures (which is often coincident with heavy telluric contamination). Spectral orders that satisfy these conditions are excluded if we suspect useful information cannot be gained from the spectral order, most frequently due to telluric contamination. Many orders also exhibit what appears to be a hot component a few hundred kelvin hotter than the ambient component, which could be evidence of a facular flux component. Attempts to recover this component were unsuccessful, but perhaps worth future investigation.

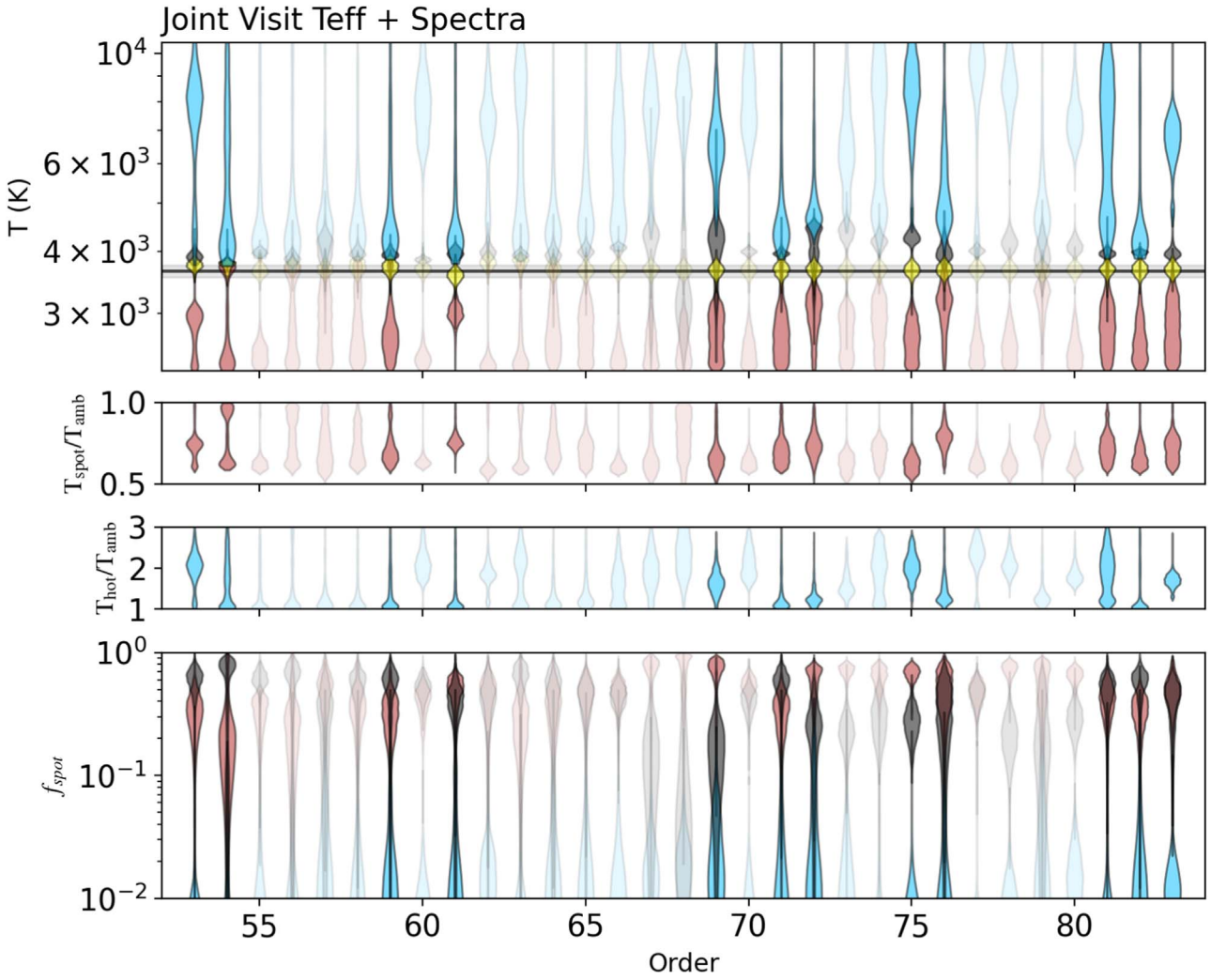

Figure 13. Combined-visit model violin plots showing the posterior distributions when modeling only the spectra and $T_{\rm eff}$. Spectral orders shown in this plot span 0.557–0.888 μm, with wavelength decreasing to the right. Top: temperature components for the hot (blue), middle (black), and spot (red) components. In yellow is the corresponding $T_{\rm eff}$. Most orders exhibit a hot component between 7000 and 10,000 K, consistent with the temperatures of flares in this wavelength range. Spot temperatures are generally poorly constrained, with the 3000 K spot seemingly detected in a handful of orders (53, 61, 72, 76, and 79). Middle: the temperature ratio, $T_{\rm spot}/T_{\rm amb}$. The five orders showing a spot solution tend to show a temperature ratio of between 0.7–0.8. Bottom: coverage fractions for the spotted (red), ambient (black), and hot (blue) components. The hot component is very small, less than 3%. There is no clear agreement with spot coverage between orders, with the largest component being the ambient photosphere in the early orders while the later (bluer) orders show a larger spot filling factor. Orders with very poor constraints tend to overlap with orders that are contaminated by tellurics. Orders omitted from the analysis are grayed out.

ORCID iDs

William C. Waalkes https://orcid.org/0000-0002-8961-0352
Zachory K. Berta-Thompson https://orcid.org/0000-0002-3321-4924
Elisabeth R. Newton https://orcid.org/0000-0003-4150-841X
Andrew W. Mann https://orcid.org/0000-0003-3654-1602
Peter Gao https://orcid.org/0000-0002-8518-9601
Hannah R. Wakeford https://orcid.org/0000-0003-4328-3867
Lili Alderson https://orcid.org/0000-0001-8703-7751
Peter Plavchan https://orcid.org/0000-0002-8864-1667

References

Afram, N., & Berdyugina, S. V. 2015, A&A, 576, A34
Afram, N., & Berdyugina, S. V. 2019, A&A, 629, A83
Ahrer, E.-M., Stevenson, K. B., Mansfield, M., et al. 2023, Natur, 614, 653
Alderson, L., Wakeford, H. R., Alam, M. K., et al. 2023, Natur, 614, 664
Allard, F. 2014, in IAU Symp. 299, Exploring the Formation and Evolution of Planetary Systems, ed. M. Booth, B. C. Matthews, & J. R. Graham (Cambridge: Cambridge Univ. Press), 271
Allard, F., Homeier, D., Freytag, B., & Sharp, C. M. 2012, in Low-Mass Stars and the Transition Stars/Brown Dwarfs, ed. C. Reylé, C. Charbonnel, & M. Schultheis, 57 (Les Ulis: EDP Sciences), 3
Angus, R., Morton, T., Aigrain, S., Foreman-Mackey, D., & Rajpaul, V. 2018, MNRAS, 474, 2094
Apai, D., Rackham, B. V., Giampapa, M. S., et al. 2018, arXiv:1803.08708
Astropy Collaboration, Price-Whelan, A. M., Lim, P. L., et al. 2022, ApJ, 935, 167
Astropy Collaboration, Price-Whelan, A. M., Sipőcz, B. M., et al. 2018, AJ, 156, 123
Astropy Collaboration, Robitaille, T. P., Tollerud, E. J., et al. 2013, A&A, 558, A33
Barclay, T., Sheppard, K. B., Latouf, N., et al. 2023, arXiv:2301.10866
Basri, G. 2021, An Introduction to Stellar Magnetic Activity (Bristol: IOP Publishing), 164
Berardo, D., de Wit, J., & Rackham, B. V. 2024, ApJL, 961, L18
Berdyugina, S. V. 2005, LRSP, 2, 8
Berdyugina, S. V., Berdyugin, A. V., Fluri, D. M., & Piirola, V. 2011, ApJL, 728, L6
Berta, Z. K., Charbonneau, D., Désert, J.-M., et al. 2012, ApJ, 747, 35
Brown, T. M., Charbonneau, D., Gilliland, R. L., Noyes, R. W., & Burrows, A. 2001, ApJ, 552, 699
Cao, L., Pinsonneault, M. H., Hillenbrand, L. A., & Kuhn, M. A. 2022, ApJ, 924, 84
Chen, C. H., Patten, B. M., Werner, M. W., et al. 2005, ApJ, 634, 1372
Collins, K. A., Kielkopf, J. F., Stassun, K. G., & Hessman, F. V. 2017, AJ, 153, 77
Cristofari, P. I., Donati, J. F., Folsom, C. P., et al. 2023, MNRAS, 522, 1342
Donati, J. F., Cristofari, P. I., Finociety, B., et al. 2023, MNRAS, 525, 455
Feinstein, A. D., France, K., Youngblood, A., et al. 2022, AJ, 164, 110
Feinstein, A. D., Radica, M., Welbanks, L., et al. 2023, Natur, 614, 670
Flagg, L., Johns-Krull, C. M., France, K., et al. 2022, ApJ, 934, 8
Foreman-Mackey, D., Hogg, D. W., Lang, D., & Goodman, J. 2013, PASP, 125, 306
Fu, G., Espinoza, N., Sing, D. K., et al. 2022, ApJL, 940, L35
Gaia Collaboration, Vallenari, A., Brown, A. G. A., et al. 2023, A&A, 674, A1
Gilbert, E. A., Barclay, T., Quintana, E. V., et al. 2022, AJ, 163, 147
Goodman, J, & Weare, J 2010, Commun. Appl. Math. Comput. Sci., 5, 65
Gray, D. F. 1984, ApJ, 277, 640
Gully-Santiago, M. A., Herczeg, G. J., Czekala, I., et al. 2017, ApJ, 836, 200
Herbst, K., Papaioannou, A., Airapetian, V. S., & Atri, D. 2021, ApJ, 907, 89
Hirano, T., Krishnamurthy, V., Gaidos, E., et al. 2020, ApJL, 899, L13
Hunter, J. D. 2007, CSE, 9, 90
Husser, T.-O., Wende-von Berg, S., Dreizler, S., et al. 2013, A&A, 553, A6
Ikuta, K., Namekata, K., Notsu, Y., et al. 2023, ApJ, 948, 64
Iyer, A. R., & Line, M. R. 2020, ApJ, 889, 78
Iyer, A. R., Line, M. R., Muirhead, P. S., Fortney, J. J., & Gharib-Nezhad, E. 2023, ApJ, 944, 41
Jones, A., Noll, S., Kausch, W., Szyszka, C., & Kimeswenger, S. 2013, A&A, 560, A91
Jones, H. R. A., Longmore, A. J., Allard, F., et al. 1995, MNRAS, 277, 767
Kalas, P., Liu, M. C., & Matthews, B. C. 2004, Sci, 303, 1990
Libby-Roberts, J. E., Berta-Thompson, Z. K., Diamond-Lowe, H., et al. 2022, AJ, 164, 59
Lim, O., Benneke, B., Doyon, R., et al. 2023, ApJL, 955, L22
Louca, A. J., Miguel, Y., Tsai, S.-M., et al. 2023, MNRAS, 521, 3333
MacGregor, M. A., Wilner, D. J., Rosenfeld, K. A., et al. 2013, ApJL, 762, L21
Mamajek, E. E., & Bell, C. P. M. 2014, MNRAS, 445, 2169
Martioli, E., Hébrard, G., Correia, A. C. M., Laskar, J., & Lecavelier des Etangs, A. 2021, A&A, 649, A177
McCully, C., Turner, M., Collom, D., & Daily, M., 2022 BANZAI: Beautiful Algorithms to Normalize Zillions of Astronomical Images, Astrophysics Source Code Library, ascl:2207.031
Medina, A. A., Charbonneau, D., Winters, J. G., Irwin, J., & Mink, J. 2022, ApJ, 928, 185
Mikal-Evans, T., Madhusudhan, N., Dittmann, J., et al. 2023, AJ, 165, 84
Moran, S. E., Stevenson, K. B., Sing, D. K., et al. 2023, ApJL, 948, L11
Neff, J. E., O'Neal, D., & Saar, S. H. 1995, ApJ, 452, 879
Noll, S., Kausch, W., Barden, M., et al. 2012, A&A, 543, A92
Norris, C. M., Unruh, Y. C., Witzke, V., et al. 2023, MNRAS, 524, 1139
Olah, K., Kővári, Z., Bartus, J., et al. 1997, A&A, 321, 811
Pass, E. K., Winters, J. G., Charbonneau, D., Irwin, J. M., & Medina, A. A. 2023, AJ, 166, 16
Plavchan, P., Barclay, T., Gagné, J., et al. 2020, Natur, 582, 497
Pont, F., Gilliland, R. L., Moutou, C., et al. 2007, A&A, 476, 1347
Pont, F., Knutson, H., Gilliland, R. L., Moutou, C., & Charbonneau, D. 2008, MNRAS, 385, 109
Rackham, B. V., Apai, D., & Giampapa, M. S. 2018, ApJ, 853, 122
Rackham, B. V., Apai, D., & Giampapa, M. S. 2019, AJ, 157, 96
Rackham, B. V., & de Wit, J. 2023, arXiv:2303.15418
Ramsey, L. W., & Nations, H. L. 1980, ApJL, 239, L121
Reiners, A., Shulyak, D., Anglada-Escudé, G., et al. 2013, A&A, 552, A103
Robertson, P., Stefansson, G., Mahadevan, S., et al. 2020, ApJ, 897, 125
Robinson, T. D., Maltagliati, L., Marley, M. S., & Fortney, J. J. 2014, PNAS, 111, 9042
Rustamkulov, Z., Sing, D. K., Mukherjee, S., et al. 2023, Natur, 614, 659
Sanchis-Ojeda, R., & Winn, J. N. 2011, ApJ, 743, 61
Schöfer, P., Jeffers, S. V., Reiners, A., et al. 2019, A&A, 623, A44
Seager, S., & Sasselov, D. D. 2000, ApJ, 537, 916
Seager, S., Whitney, B. A., & Sasselov, D. D. 2000, ApJ, 540, 504
Shapiro, A. I., Solanki, S. K., Krivova, N. A., Yeo, K. L., & Schmutz, W. K. 2016, A&A, 589, A46
Shields, A. L., Ballard, S., & Johnson, J. A. 2016, PhR, 663, 1
Sing, D. K., Fortney, J. J., Nikolov, N., et al. 2016, Natur, 529, 59
Sing, D. K., Pont, F., Aigrain, S., et al. 2011, MNRAS, 416, 1443
Strassmeier, K. G., & Olah, K. 1992, A&A, 259, 595
Szabó, G. M., Gandolfi, D., Brandeker, A., et al. 2021, A&A, 654, A159
Szabó, G. M., Garai, Z., Brandeker, A., et al. 2022, A&A, 659, L7
Thao, P. C., Mann, A. W., Gao, P., et al. 2023, AJ, 165, 23
The pandas development team, 2024 pandas-dev/pandas: Pandas, v2.2.0, Zenodo, doi:10.5281/zenodo.10537285
Torres, C. A. O., & Ferraz Mello, S. 1973, A&A, 27, 231
van der Walt, S., Colbert, S. C., & Varoquaux, G. 2011, CSE, 13, 22
Vogt, S. S. 1979, PASP, 91, 616
Vogt, S. S. 1981, ApJ, 250, 327
Wakeford, H. R., Lewis, N. K., Fowler, J., et al. 2019, AJ, 157, 11
Wing, R. F., Peimbert, M., & Spinrad, H. 1967, PASP, 79, 351
Wittrock, J. M., Dreizler, S., Reefe, M. A., et al. 2022, AJ, 164, 27
Wittrock, J. M., Plavchan, P., Cale, B. L., et al. 2023, AJ, 166, 232
Yamashita, M., Itoh, Y., & Oasa, Y. 2022, PASJ, 74, 1295
Zacharias, N., Finch, C. T., Girard, T. M., et al. 2012, yCat, I/322A
Zhang, Z., Zhou, Y., Rackham, B. V., & Apai, D. 2018, AJ, 156, 178
Zicher, N., Barragán, O., Klein, B., et al. 2022, MNRAS, 512, 3060